DISEASES AND DISORDERS

PPDPF preserves integrity of proximal tubule by modulating NMNAT activity in chronic kidney diseases

Xiaoliang Fang[1]†, Yi Zhong[2]†, Rui Zheng[1]†, Qihui Wu[3]†, Yu Liu[3], Dexin Zhang[4], Yuwei Wang[3], Wubing Ding[5], Kaiyuan Wang[2], Fengbo Zhong[2], Kai Lin[2], Xiaohui Yao[6,7], Qingxun Hu[8], Xiaofei Li[9], Guofeng Xu[4], Na Liu[10], Jing Nie[11], Dali Li[2], Hongquan Geng[1]*, Yuting Guan[2,12]*

Genome-wide association studies (GWAS) have identified loci associated with kidney diseases, but the causal variants, genes, and pathways involved remain elusive. Here, we identified a kidney disease gene called pancreatic progenitor cell differentiation and proliferation factor (PPDPF) through integrating GWAS on kidney function and multiomic analysis. PPDPF was predominantly expressed in healthy proximal tubules of human and mouse kidneys via single-cell analysis. Further investigations revealed that PPDPF functioned as a thiol-disulfide oxidoreductase to maintain cellular NAD$^+$ levels. Deficiency in PPDPF disrupted NAD$^+$ and mitochondrial homeostasis by impairing the activities of nicotinamide mononucleotide adenylyl transferases (NMNATs), thereby compromising the function of proximal tubules during injuries. Consequently, knockout of PPDPF notably accelerated the progression of chronic kidney disease (CKD) in mouse models induced by aging, chemical exposure, and obstruction. These findings strongly support targeting PPDPF as a potential therapy for kidney fibrosis, offering possibilities for future CKD interventions.

INTRODUCTION

The global prevalence of chronic kidney disease (CKD) is approximately 15%, making it the ninth leading cause of death worldwide (*1*, *2*). However, effective therapies to slow down CKD progression are lacking, resulting in an increasing number of patients being diagnosed with fatal end-stage renal disease. Despite decades of mechanistic studies on CKD, the genes and molecular pathways involved in its early stages remain incompletely understood and require further investigation. Although genome-wide association analyses (GWAS) have identified nearly 800 loci associated with kidney function in large populations (*3*–*7*), the specific cell types and underlying molecular mechanisms remain unresolved since more than 90% of GWAS-identified variants are noncoding (*8*).

Recent genetic studies, such as GWAS and multiomic studies, have highlighted the importance of proximal tubule (PT)–specific genes in renal pathophysiology (*5*, *9*–*11*). Because of their high vulnerability during renal dysfunctions (*12*, *13*), PT cells rapidly respond to tubule fluid flow, intracavitary pressure, wall tension, and matrix hardness alterations, which then accordingly regulate the genomic transcriptions involved in cell proliferation, differentiation, and apoptosis (*14*, *15*). Moreover, PT injury has been demonstrated in the early stages of diabetic kidney disease (DKD) and promotes DKD progression (*16*). Therefore, understanding the initial cellular events driving kidney fibrosis would expand our knowledge of CKD and help develop new therapeutic strategies.

PPDPF, also known as pancreatic progenitor cell differentiation and proliferation factor, is widely distributed in various organs and plays essential roles in multiple physiological and pathological processes. For instance, it promotes lung adenocarcinoma progression via inhibiting apoptosis and natural killer cell–mediated cytotoxicity (*17*). In addition, knockout (KO) of *PPDPF* significantly suppresses the development of pancreatic ductal adenocarcinoma driven by kirsten rat sarcoma viral oncogene homologue (KRAS) mutation (*18*). While in nontumor studies, *PPDPF* prevents Raptor ubiquitination and activation by inhibiting the interaction between Raptor and CUL4B-DDB1, thereby reducing lipid synthesis and ameliorating fatty liver development (*19*). Recently, a GWAS meta-analysis involving creatinine-based estimated glomerular filtration rate (eGFR) from the Chronic Kidney Disease Genetics Consortium and UK Biobank (n = 1,201,909) revealed that *PPDPF* is highly relevant to kidney function (*20*). The risk allele of GWAS eGFR single-nucleotide polymorphisms was associated with expression changes of *PPDPF* in bulk expression quantitative trait loci (eQTL) (*21*), cell fraction eQTL (*22*), as well as meta-eQTL analysis (*7*) of human kidney samples. However, the molecular mechanisms between *PPDPF* and renal injuries remain largely unexplored.

In this study, our aim was to identify genes and pathways that drive kidney fibrogenesis from the earliest cellular events. To address this issue, we analyzed the early-stage transcriptomes of CKD tissues at both bulk and single-cell resolutions. Single-cell transcriptomic analysis unveiled a marked up-regulation of *PPDPF*, a top

---

[1] Department of Urology, Children's Hospital of Fudan University, Shanghai, 201102, China. [2] Shanghai Frontiers Science Center of Genome Editing and Cell Therapy, Shanghai Key Laboratory of Regulatory Biology, Institute of Biomedical Sciences and School of Life Sciences, East China Normal University, Shanghai, 200241, China. [3] Shanghai Key Laboratory of Anesthesiology and Brain Functional Modulation, Clinical Research Center for Anesthesiology and Perioperative Medicine, Translational Research Institute of Brain and Brain-Like Intelligence, Shanghai Fourth People's Hospital, School of Medicine, Tongji University, Shanghai, 200434, China. [4] Department of Pediatric Urology, Xinhua Hospital Affiliated to Shanghai Jiao Tong University School of Medicine, Shanghai, 200092, China. [5] Genomic Analysis Laboratory, The Salk Institute for Biological Studies, La Jolla, CA 92037, USA. [6] Qingdao Innovation and Development Center, Harbin Engineering University, Qingdao, Shandong, 266000, China. [7] College of Intelligent Systems Science and Engineering, Harbin Engineering University, Harbin, Heilongjiang, 150001, China. [8] Shanghai Engineering Research Center of Organ Repair, School of Medicine, Shanghai University, Shanghai, 200444, China. [9] Division of Neurogeriatrics, Department of Neurobiology, Care Sciences and Society, Karolinska Institutet, Stockholm, 17164, Sweden. [10] Department of Nephrology, Shanghai East Hospital, Tongji University School of Medicine, Shanghai, 200120, China. [11] Biobank of Peking University First Hospital, Peking University First Hospital, Peking University, Beijing, 100034, China. [12] Chongqing Key Laboratory of Precision Optics, Chongqing Institute of East China Normal University, Chongqing, 401120, China.
*Corresponding author. Email: ytguan@bio.ecnu.edu.cn (Y.G.); genghongquan@fudan.edu.cn (H.G.)
†These authors contributed equally to this work.

target of kidney function GWAS, in the healthy PT subgroup during early stages of CKD in human and mouse. *Ppdpf* deficiency results in mitochondrial dysregulation by inhibiting nicotinamide mononucleotide (NMN) conversion into NAD$^+$. Mechanistically, PPDPF functions as a thiol-disulfide oxidoreductase during this conversion process to maintain the activity of nicotinamide mononucleotide adenylyl transferases (NMNATs). Consistently, KO of *Ppdpf* aggravates aging-, cisplatin-, unilateral ureteral obstruction (UUO)–, and folic acid (FA)–induced mouse CKD models, while supplementation with nicotinamide adenine dinucleotide (oxidized form; NAD$^+$) but not NMN alleviates renal dysfunctions. Last, adeno-associated virus-mediated overexpression of *Ppdpf* protects against renal injuries in vivo. Our studies suggest that PPDPF is a regulator of NAD$^+$ homeostasis involved in modulating CKD progression and could be an effective therapeutic target.

RESULTS

Single-cell and GWAS identify *PPDPF* as a kidney disease risk gene

To investigate gene expression profiles associated with early stages of kidney fibrosis, we initially conducted bulk RNA sequencing (RNA-seq) on kidneys at day 1 and day 5 post-UUO surgery (Fig. 1A). The UUO models were well-characterized, showing kidney structural damage and the expression of kidney injury markers *Havcr1*, *Lcn2*, and *Vimentin* (fig. S1, A and B). Principal components analysis (PCA) indicated gene expression clustering among control, UUO 1-day (1d), and UUO 5-day (5d) groups (fig. S1C). Differential expression analysis identified 2052 differentially expressed genes (DEGs) in UUO 1d (1027 up-regulated and 1025 down-regulated), as well as 3114 DEGs in UUO 5d compared to the controls (1752 up-regulated and 1362 down-regulated) (fig. S1D). The volcano plots highlighted DEGs that exhibited significant changes exclusively in UUO 1d but not in UUO 5d. In total, nearly a thousand genes were identified during the initial progression of kidney fibrosis (488 increased and 490 decreased DEGs, respectively) (Fig. 1B).

Next, single-cell RNA-seq (scRNA-seq) was performed to further explore the cellular changes at early stages of kidney fibrosis. A total of 43,257 individual cells were analyzed from three control kidneys, three UUO 1d kidneys, and two UUO 5d kidneys. Cell clustering analysis revealed 18 major cell types based on the expression patterns of marker genes (Fig. 1C and fig. S1E). Through the scRNA-seq data, we observed marked alterations in cell proportions at day 1, including increased ratios of immune cells such as macrophages (1.8-fold), B cells (8.9-fold), T cells (4.63-fold), natural killer cells (3.6-fold), and neutrophils (56.5-fold) (fig. S1F). There was a notable decrease in PT cells on day 1 (8-fold) despite concurrent increases seen in other epithelial cell types like loop of Henle (7.3-fold), distal convoluted tubule (4.1-fold), principal cell (4.8-fold), and intercalated cell (5.1-fold) (fig. S1F). Furthermore, the significantly changed genes on day 1 in bulk RNA-seq were enriched in PT cells of scRNA-seq dataset (Fig. 1D). In particular, differential expression analysis of PT cells on UUO 1d from scRNA-seq data identified 955 DEGs (502 up-regulated and 453 down-regulated) (fig. S1G). This combined analysis of bulk seq and scRNA-seq dataset suggests a significant involvement of PT cells in driving transcriptomic changes during the early stages of kidney fibrosis.

To further narrow down the candidates involved in the onset or regulation of kidney injury, we performed an overlapping analysis of up-regulated DEGs in PT on UUO 1d from scRNA-seq, up-regulated DEGs on UUO 1d from bulk RNA-seq, as well as prioritized target genes of kidney function GWAS identified through meta-analysis of publicly available datasets from CKDGen, Pan-UK Biobank, Million Veteran Program (MVP), Population Architecture Using Genomics and Epidemiology (PAGE), Surrogate Markers for Micro- and Macrovascular Hard Endpoints for Innovative Diabetes Tools (SUMMIT) consortia (*7*). This analysis identified seven genes: *PPDPF*, *CALR*, *STAT3*, *NDRG1*, *SLC2A2*, *UHRF2*, and *COMT* (Fig. 1E). Among these genes, *CALR* and *STAT3* have been reported as important modulators of kidney fibrosis development (*23*, *24*). Despite having the highest priority score in eGFR GWAS locus, there has been no previous experimental research specifically addressing PPDPF in CKD. We then prioritized the eGFRcrea GWAS locus on chromosome 20, where omic datasets and statistical models identified causal variants underlying kidney function and target gene *PPDPF* (fig. S1H). Other GWAS have also consistently associated the region on chromosome 20 tagged by rs72629024 with kidney function (eGFR) (*5*, *20*). The effect allele G of rs72629024 is associated with lower GFR in the GWAS. The top prioritized variant rs72629024 showed significant association with kidney function (eGFRcrea GWAS, z score = −9.661, $P = 4.43 \times 10^{-22}$) and *PPDPF* expression [eQTL (*25*), $\beta = -0.416$, $P = 4.365 \times 10^{-14}$; eQTL(cf) (*22*), $\beta = -0.652$, $P = 2.011 \times 10^{-34}$ (fig. S1I); eQTL(meta) (*7*), $\beta = -0.5834$, $P = 5.39 \times 10^{-54}$]. Overall, these results suggest that rs72629024 has kidney-specific eQTL effects, prioritized *PPDPF* as a gene associated with kidney disease.

The expression of *Ppdpf* was confirmed at both transcriptomic and protein levels in mouse models induced by cisplatin, FA, and ischemia reperfusion injury (IRI). All these models showed elevated *Ppdpf* expression levels (Fig. 1, F and G). A higher signal of PPDPF was observed in tubules with relative low levels of KIM1 (Fig. 1H and fig. S1J), a marker for renal tubule injury. Consistently, the expression levels of *PPDPF* increased in human kidney samples of acute kidney injury (AKI) from publicly available scRNA-seq and bulk seq datasets (Fig. 1I) (*26*, *27*). Regardless of this increase during AKI or the early stage of fibrosis, dynamic changes of *Ppdpf* were also observed during the progression of CKD, as characterized by an increase on day 1 followed by a subsequent decrease on day 28 in FA models (fig. S1K). In addition, another scRNA-seq conducted on long-term kidney injury samples confirmed that reduced expression of *Ppdpf* in the late stage of kidney injury (fig. S2, A to E). In line with the UUO model, *Ppdpf* was enriched in PT but exhibited a marked decrease following a 7-day treatment (fig. S2, F and G). The collective findings suggest that *Ppdpf* is a susceptibility gene for kidney diseases and exhibits up-regulated expression levels during the initial stages, indicating its role as a renal protective factor.

Ppdpf is mainly expressed in the healthy subcluster of PT

We further examined *Ppdpf* expression in PT subclusters and found a consistent increase followed by a decrease pattern, as shown in both our and published scRNA-seq datasets (Fig. 2, A and B) (*26*). Moreover, isolated LTL-positive PT cells from UUO 1d mouse kidneys confirmed up-regulation of *Ppdpf* at transcript and protein levels (Fig. 2, C and D).

To better understand the role of *Ppdpf* in PT cells, we subclustered healthy and diseased samples from UUO kidneys. We identified eight subtypes of PT using publicly available markers (*10*, *26*, *28*). These subtypes included proximal convoluted tubule (S1) expressing *Slc5a12*,

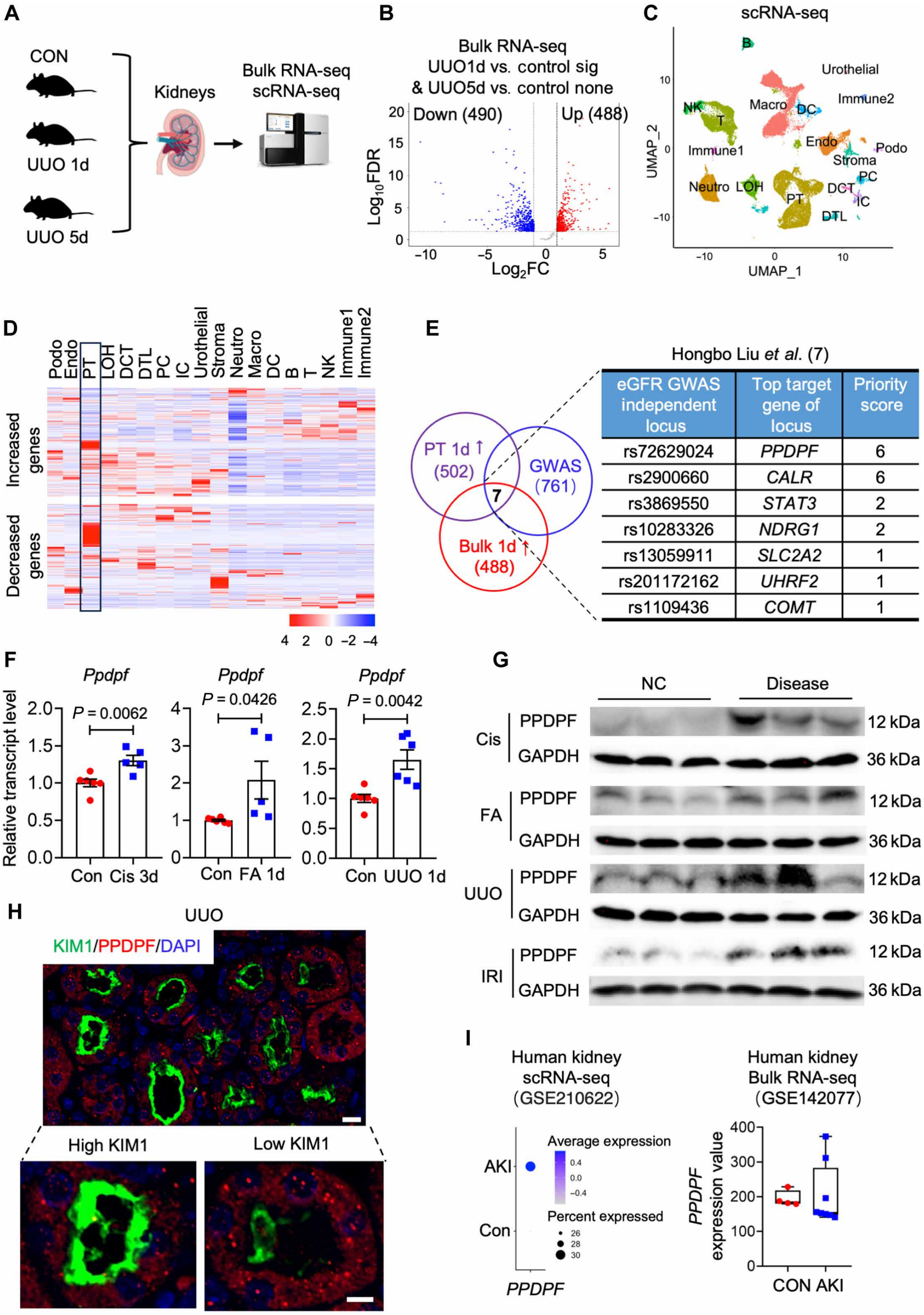

Hongbo Liu *et al.* (7)

eGFR GWAS independent locus	Top target gene of locus	Priority score
rs72629024	*PPDPF*	6
rs2900660	*CALR*	6
rs3869550	*STAT3*	2
rs10283326	*NDRG1*	2
rs13059911	*SLC2A2*	1
rs201172162	*UHRF2*	1
rs1109436	*COMT*	1

Fig. 1. The kidney disease risk gene, *PPDPF*, was up-regulated in the early stages of both human and mouse kidney diseases. (**A**) Schematic representation of bulk RNA-seq and scRNA-seq on kidney samples of 1d and 5d UUO. (**B**) DEGs that were significant in UUO 1d but not significant in UUO 5d of bulk RNA-seq. (**C**) The UMAP of 18 distinct cell types identified by unsupervised clustering. Endo, endothelial cell; podo, podocyte; LOH, loop of Henle; DTL, descending thin limb of Henle's loop; DCT, distal convoluted tubule; PC, principal cell; IC, intercalated cell; urothelial, urothelial cell; macro, macrophage; B, B lymphocyte; NK, natural killer cell; T, T cell; neutro, neutrophile; DC, dendritic cell; stroma, stroma cell; Immune1, immune cell type 1; Immune2, immune cell type 2. (**D**) Cell type–specific expression of top DEGs identified from (B). (**E**) Venn diagram exhibits the overlaps among indicated sets (up arrow: up-regulated DEGs). (**F**) The relative mRNA expression of *Ppdpf* in the cisplatin (Cis)–, FA-, and UUO-administered kidney samples. (**G**) Western blots of PPDPF in Cis-, FA-, UUO-, and IRI-administered kidney samples. Eight-week-old male mice were used. NC, negative control. (**H**) Representative images of double staining of PPDPF and KIM1 in the UUO-administered kidneys. Scale bar, 20 μm. (**I**) The relative mRNA expression of *PPDPF* in human AKI kidneys. P value was calculated by two-tailed t test. $P < 0.05$ is statistically significant. Data are represented as mean ± SEM. (A to D) $n = 3$, control; $n = 3$, UUO 1d mice; $n = 2$, UUO 5d mice. (F) For Cis: $n = 6$, control; $n = 5$, Cis-treated mice. For FA: $n = 6$, control; $n = 5$, FA-treated mice. For UUO: $n = 6$, control; $n = 6$, UUO-treated mice. (G) Three control mice and three diseased mice were included for each model. FC, fold change; GAPDH, glyceraldehyde phosphate dehydrogenase; DAPI, 4′,6-diamidino-2-phenylindole.

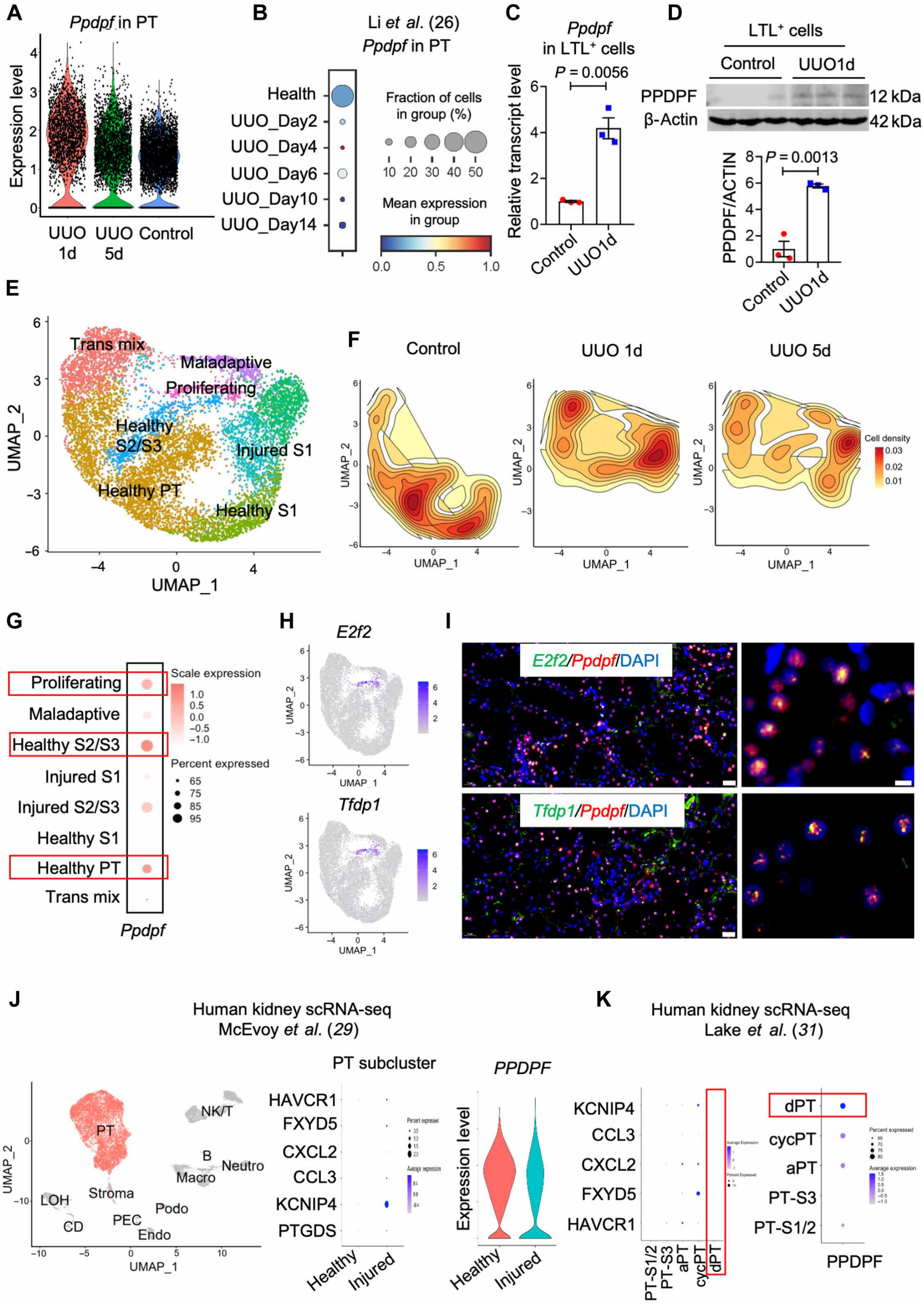

Fig. 2. *Ppdpf* is mainly expressed in the healthy PT subclusters. (**A**) Expression of *Ppdpf* in the PT of control, UUO 1d, and UUO 5d mouse kidneys by scRNA-seq. (**B**) Bubble plot of *Ppdpf* expression in PT clusters of UUO by scRNA-seq (GSE190887). (**C**) Expression of *Ppdpf* in isolated LTL$^+$ cells from control and UUO 1d. (**D**) Top: Western blots of PPDPF in isolated LTL$^+$ cells from control and UUO 1d. Bottom: Western blots quantification. (**E**) UMAP of all PT cells in subclustering analysis. (**F**) UMAP of cell densities of PT cells between different treatment groups. (**G**) Bubble plot of *Ppdpf* expression in each subcluster of (E). (**H**) Feature plots of *E2f2* (proliferating PT) and *Tfdp1* (proliferating PT). (**I**) Representative FISH images. Scale bars, 20 μm. (**J**) Expression of *PPDPF* in the scRNA-seq of human kidneys (GSE202109). Left: UMAP of human kidney with cell type annotations. PEC, pericyte; CD, collecting duct. Middle: Bubble plots of injured cell cluster marker genes. Right: Expression of *PPDPF* in PT subcluster. (**K**) Expression of *PPDPF* in the scRNA-seq of human kidneys (GSE183276). Left: Bubble plots of injured cell cluster marker genes; right: *PPDPF* expression in PT subcluster. *P* value was calculated by two-tailed *t* test. $P < 0.05$ is statistically significant. Data are represented as mean ± SEM. (A) $n = 3$, control; $n = 3$, UUO 1d mice; $n = 2$, UUO 5d mice. (C) $n = 3$, control; $n = 3$, UUO 1d mice. (D) $n = 3$, control; $n = 3$, UUO 1d mice.

proximal straight tubule (S2/S3) expressing *Slc7a13*, injured PT subcluster expressing *Havcr1*, *Ptgds*, and *Hsp90aa1*, proliferating PT expressing *Top2a*, and transient mixed PT expressing *Wfdc15b* (Fig. 2E and fig. S3A). In addition, we found a proinflammatory subcluster previously reported as maladaptive PT that expresses various chemokines (*Fxyd5*, *Cxcl2*, and *Ccl3*) (Fig. 2E and fig. S3A) (*28*). The clustering analysis revealed limited correlation between injured and healthy PT cells (fig. S3B). The changes in cell density were analyzed to address the issue of artificially clustering cells. Control samples showed the highest cell density in healthy PT clusters, while UUO samples exhibited increased density in injured clusters on day 1 after surgery (Fig. 2F). Both injured and maladaptive PT displayed strong enrichment in proinflammatory pathways like JAK-Stat, tumor necrosis factor, and nuclear factor κB but showed weak signals in anti-inflammatory pathways such as vascular endothelial growth factor and Wingless/Integrated (WNT) signaling (fig. S3C). *Ppdpf* exhibited high expression levels within healthy clusters (proliferating PT, healthy S2/S3, and healthy PT) (Fig. 2G), consistent with a study by Humphreys' group (fig. S3D) (*26*). Moreover, fluorescent in situ hybridization (FISH) results demonstrated the colocalization of *Ppdpf* with two transcription factors *E2f2* and *Tfdp1* specifically expressed within the proliferating subgroup based on scRNA-seq analysis (Fig. 2, H and I). To further investigate the origin of increased *Ppdpf* expression, we isolated healthy and injured PT cells from sham and UUO kidneys using LTL microbeads and KIM1 antibody with anti-rabbit microbeads (fig. S3E). Our findings revealed that *Ppdpf* expression in the KIM1-negative PT cells of UUO kidneys was higher compared to sham kidneys (fig. S3F), indicating that the up-regulation of *Ppdpf* during early-stage kidney injury mainly originated from healthy PT cells rather than injured ones, regardless of their abundance. These results provide strong evidence for both localization and up-regulation of *Ppdpf* within healthy PT cells.

To further validate our findings on *PPDPF* expression in clinical samples, we reanalyzed three different scRNA-seq datasets of human kidneys. The first dataset consisted of preimplantation kidney samples from 19 donors (*29*), revealing 11 distinct subpopulations with higher PPDPF expression observed in the healthy PT subcluster compared to the injured one (Fig. 2J and fig. S3G). Similar results were found in the second dataset collected from cryopreserved human diabetic kidney samples (fig. S3H) (*30*). The third study using single-cell and single-nucleus multiomic techniques profiled more than 400,000 cells, and nuclei from human kidneys (*31*) also confirmed that *PPDPF* exhibited high expression in a degenerative PT (dPT) subcluster with minimal expression of injured and immune markers *KCNIP*, *CXCL2*, *FXYD5*, and *HAVCR1* (Fig. 2K). Thus, these scRNA-seq analyses of human kidney confirmed that PPDPF was predominantly expressed in "healthy" PT cells as observed in animal models (Fig. 2G).

Disruption of *Ppdpf* impairs mitochondrial homeostasis

To assess the activated molecular pathways in UUO 1d kidneys, we initially examined whether stress responses were enhanced in PT cells. While the tissue damage–induced 98 stress responsive genes (*32*) showed a significant increase in UUO 1d, there was no enrichment of the stress score in the PT segment (Fig. 3, A and B). Conversely, DEGs of PT on UUO 1d exhibited enrichment for metabolic pathways instead (Fig. 3C).

To investigate the potential role of *PPDPF* in metabolism, we performed knockdown using small interfering RNA (siRNA) in human embryonic kidney (HEK) 293T cells and KO using CRISPR-Cas9 techniques in human PT HK2 cells, respectively. The efficiency was confirmed by quantitative polymerase chain reaction (qPCR) and Western blot in HEK293T cells (fig. S4, A and B) and human PT HK2 cells (fig. S4, C and D). Deficiency of *PPDPF* led to a significant increase in LDH release in both cell types (fig. S4, E and F). Furthermore, transfection with siPPDPF or sgPPDPF disrupted mitochondrial membrane potential and reactive oxygen species levels, as assessed by JC1 and mitoSOX dyes (fig. S4, G to J).

To investigate the role of *Ppdpf* in kidney tissues, we used CRISPR-Cas9 technique to generate *Ppdpf* KO mice (fig. S5A) (*33*). The *Ppdpf* KO mice were born at the expected Mendelian ratio and appeared phenotypically normal. The successful generation of the *Ppdpf* KO mice was confirmed by analyzing transcript and protein expressions in kidney tissues (fig. S5, B and C). The specificity of the PPDPF antibody was also confirmed through staining, which revealed a robust punctate pattern of PPDPF expression in wild-type (WT) kidneys. In contrast, this pattern was not observed in KO kidneys or negative control kidneys that were only treated with a secondary antibody (fig. S5D). Moreover, most blood biochemical parameters, including creatinine, blood urea nitrogen (BUN), electrolytes, and kidney segment markers in KO mice, showed similar levels to those of WT, except for a significant increase in *Lcn2* observed in KO kidneys (fig. S6, A and B), indicating potential kidney injuries of the KO mice.

Electron microscopy (EM) analysis showed that mitochondria in *Ppdpf* KO kidneys exhibited enlarged and rounded shapes, weakened matrix, shortened cristae, widened intercristal space, and vacuoles of varying sizes compared to WT (Fig. 3, D and E), indicating progressive structural defects. Consistently, *Ppdpf* KO led to decreased mitochondrial DNA (mtDNA) copy number and complex I activity in kidney tissues (Fig. 3, F and G). In addition, KO of *Ppdpf* also resulted in reduced expression of mitochondrial complex I in the electron transport chain, as indicated by NDUFB9 and NDUFS3 antibodies specific for complex I, along with an oxidative phosphorylation (OXPHOS) antibody cocktail (Fig. 3H and fig. S6C). Moreover, primary cells with *Ppdpf* deficiency exhibited increased fluorescence of JC1 and mitoSOX (Fig. 3I), while MitoTracker staining showed punctate and fragmented mitochondria in *Ppdpf* KO cells compared to the normal filamentous morphology observed in WT cells (Fig. 3J). In addition, *Ppdpf* deficiency impaired mitochondrial function in primary cells, as evidenced by reduced oxygen consumption rate (Fig. 3K). We also examined mitochondrial impairments in nonrenal organs due to the widespread expression of *Ppdpf* (The Human Protein Atlas). EM analysis revealed that KO mice exhibited reduced mitochondrial cristae in tissues with high levels of *Ppdpf* expression, such as the brain and intestine. However, in the heart where *Ppdpf* had moderate expression levels, KO mice showed similar mitochondrial cristae to WT mice but displayed weakened mitochondrial matrix (fig. S7A). No abnormalities were observed in DRP1 expression within these KO tissues for the lung, liver, and spleen which have low *Ppdpf* expression (fig. S7B). Overall, our findings suggest that *PPDPF* maintains mitochondrial homeostasis.

Ppdpf regulates cellular NAD$^+$ production

To investigate how *Ppdpf* maintains mitochondrial homeostasis, we performed bulk RNA-seq on WT and *Ppdpf* KO kidneys. Among the top 20 DEGs of *Ppdpf* KO versus WT, several cellular respiration genes (*Cox8b*, *Ucp1*, and *Nnt*) showed a significant decrease in *Ppdpf* KO kidneys compared to WTs (Fig. 4A). Gene set enrichment analysis (GSEA) confirmed a marked down-regulation of genes associated with mitochondrial respiratory chain complex I assembly

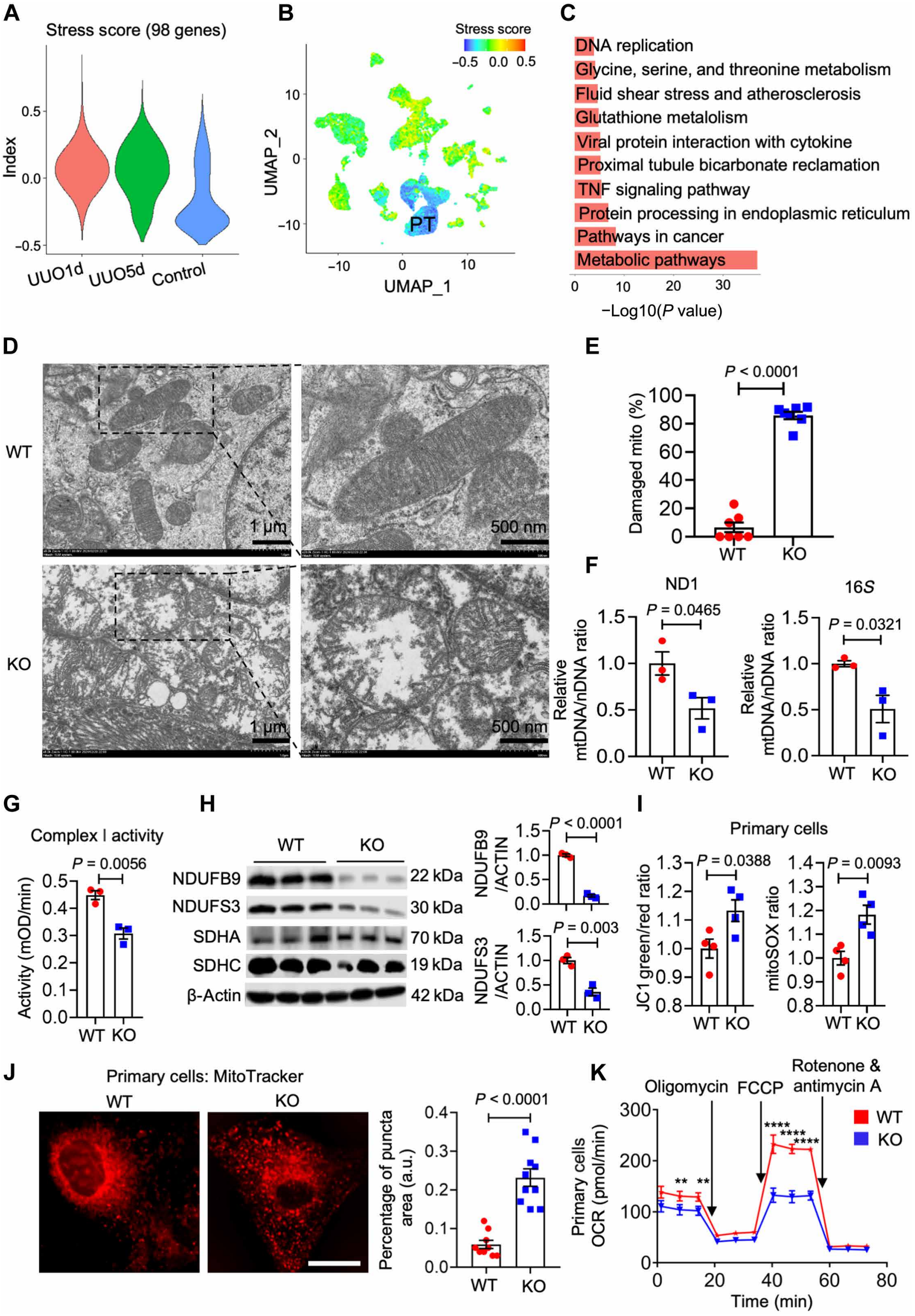

Fig. 3. Loss of *Ppdpf* impairs mitochondrial function. (**A**) The stress score of control, UUO 1d, and UUO 5d kidney samples from scRNA-seq. (**B**) UMAP plot of the stress score. (**C**) KEGG enrichment analysis in UUO 1d-specific PT cells by scRNA-seq. (**D**) Representative transmission electron microscopy images of WT and *Ppdpf* KO kidney tubules (8 weeks old). (**E**) Quantifications of damaged mitochondria in (D). (**F**) Relative mtDNA levels in WT and *Ppdpf* KO kidneys analyzed by amplifying ND1 and 16*S* genes and normalized against the hexokinase 2 (HK2) gene. (**G**) Complex I enzyme activity of kidneys from WT and *Ppdpf* KO mice. (**H**) Left: Western blots of complex I (NDUFB9 and NDUFS3) and complex II (SDHA and SDHC) in primary cells of WT and *Ppdpf* KO kidneys. Right: Quantifications of NDUFB9 and NDUFS3. (**I**) Quantifications of fluorescent JC1 signaling (green/red ratio) and fluorescent mitoSOX signaling in primary cells from WT and *Ppdpf* KO mice. (**J**) Representative images and quantifications of MitoTraker of primary cells from WT and *Ppdpf* KO mice. Scale bars, 10 μm. (**K**) Analysis of oxygen consumption rate (OCR) in primary cells from WT and *Ppdpf* KO mice. *P* value was calculated by two-tailed *t* test. $P < 0.05$ is statistically significant. Data are represented as mean ± SEM. $^{**}P < 0.01$; $^{****}P < 0.0001$. (A) $n = 3$, control; $n = 3$, UUO 1d mice; $n = 2$, UUO 5d mice. (D and E) $n = 6$, WT; $n = 6$, KO. (F to H) $n = 3$, WT; $n = 3$, KO. (I) $n = 4$, WT; $n = 4$ KO. (J) $n = 10$, WT; $n = 10$, KO. (K) $n = 3$, WT; $n = 3$, KO. TNF, tumor necrosis factor; a.u., arbitrary units; FCCP, carbonyl cyanide *p*-trifluoromethoxyphenylhydrazone; mOD, measure optical density.

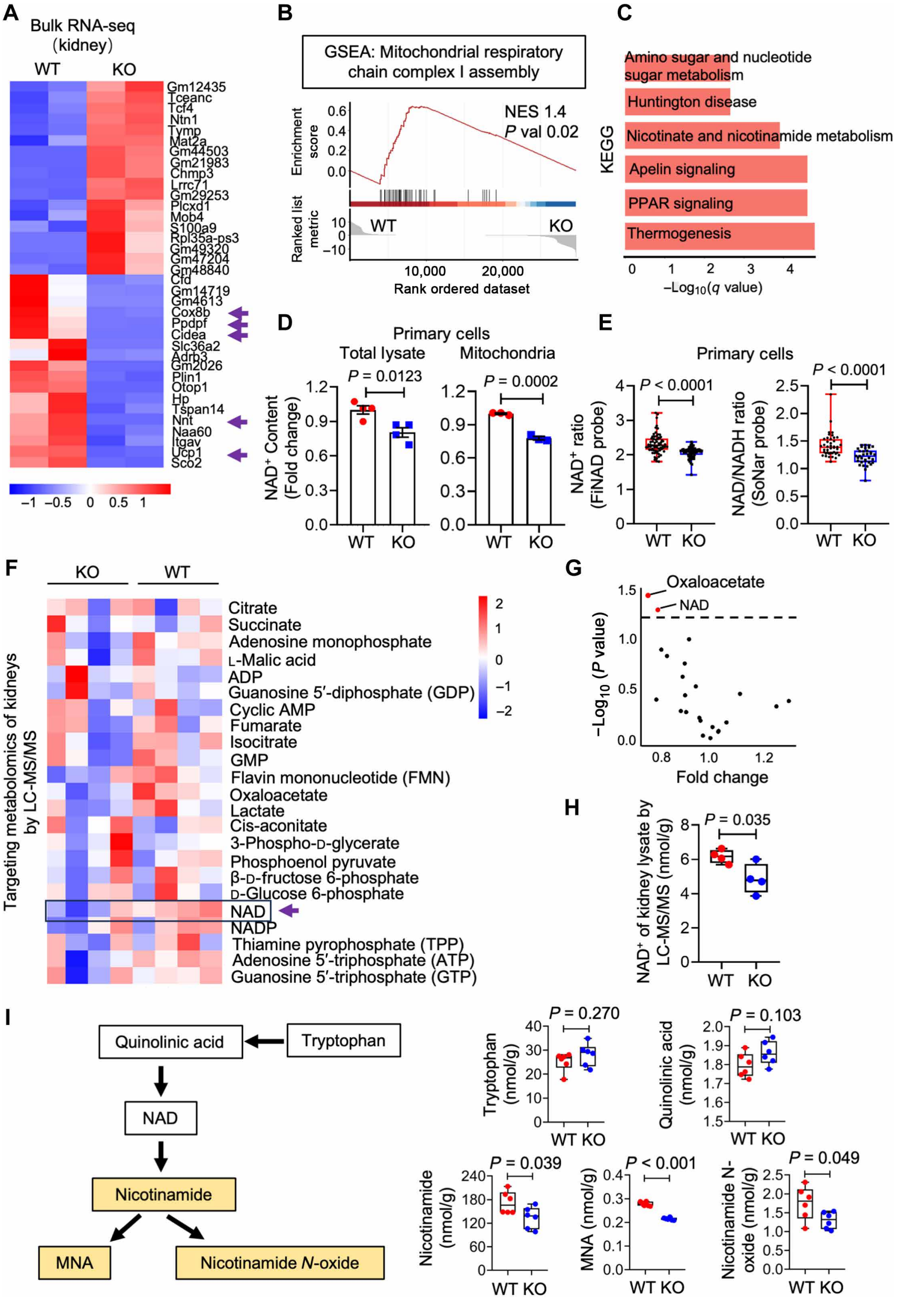

Fig. 4. *Ppdpf* regulates the cellular NAD$^+$ levels. (**A**) Heatmap of top 20 up-regulated and down-regulated genes of WT and *Ppdpf* KO kidney from bulk RNA-seq analysis. (**B**) GSEA analysis of mitochondrial respiratory chain complex I assembly from *Ppdpf* KO over WT kidneys from bulk RNA-seq data. NES, normalized enrichment score; *P* value, nominal *P* value. (**C**) KEGG enrichment analysis of DEGs from *Ppdpf* KO versus WT kidney by bulk RNA-seq. (**D**) NAD$^+$ content of whole-cell lysates and mitochondria isolated from WT and *Ppdpf* KO kidney. (**E**) Quantification of FiNad- and SoNar-positive primary cells isolated from WT and *Ppdpf* KO kidney. (**F**) Heatmap of energy metabolites of WT and *Ppdpf* KO kidneys measured by liquid chromatography–tandem mass spectrometry (LC-MS/MS). (**G**) Targeted metabolomics of *Ppdpf* KO and WT kidney measured by LC-MS/MS. Significantly changed metabolites were determined by setting a false discovery rate (FDR) of 5% and are represented in red in a volcano plot. (**H**) NAD$^+$ concentration of *Ppdpf* KO and WT kidney in targeted metabolomics measured by LC-MS/MS. (**I**) Schematic process of NAD$^+$ metabolism and quantifications of NAD$^+$ synthesis–related metabolites measured by LC-MS/MS. *P* value was calculated by two-tailed *t* test. $P < 0.05$ is statistically significant. Data are represented as mean ± SEM. (A to C) $n = 2$, WT; $n = 2$, KO. (D) For total lysate: $n = 4$, WT; $n = 4$, KO. For mitochondria: $n = 3$, WT; $n = 3$, KO. (E) For SoNar: $n = 42$, WT; $n = 34$, KO. For FiNad: $n = 67$, WT; $n = 69$, KO. (F to H) $n = 4$, WT; $n = 4$, KO. (I) $n = 6$, WT; $n = 6$, KO. PPAR, peroxisome proliferator–activated receptor; ADP, adenosine 5′-diphosphate; AMP, adenosine 5′-monophosphate; GMP, guanosine 5′-monophosphate.

in *Ppdpf* KO kidneys (Fig. 4B), consistent with previous findings on expression and activity of complex I (Fig. 3, G and H). Notably, *PPDPF* expression in human kidneys positively correlated with NDUFB6 (fig. S8A) (*34*), a gene responsible for transferring electrons from NADH to the respiratory chain within mammalian complex I. Furthermore, Kyoto Encyclopedia of Genes and Genomes (KEGG) analysis showed a strong correlation with nicotinate and nicotinamide metabolism (Fig. 4C), suggesting potential involvement of *Ppdpf* in NAD^+ biosynthesis.

To test this hypothesis, we measured NAD^+ levels in total and mitochondrial lysates from HEK293T, HK2, and primary cells. We consistently observed a decrease in NAD^+ levels across all tested cell types after knocking out *Ppdpf* (Fig. 4D and fig. S8, B and C). To avoid potential tissue contaminations during isolation, we used two genetically encoded fluorescent biosensors, FiNad (*35*) and SoNar (*36*), to visualize NAD^+ levels within living cells. Both FiNad and SoNar probes detected a decline in free NAD^+ levels in *Ppdpf* KO cells compared to WTs (Fig. 4E). Notably, targeted metabolomic studies using high-performance liquid chromatography–tandem mass spectrometry (MS/MS) revealed that only NAD^+ and oxaloacetate exhibited a significant decrease among the 21 tested metabolites in total lysates of *Ppdpf* KO kidneys (Fig. 4, F to H, and fig. S8D). In addition, our liquid chromatography–MS/MS (LC-MS/MS)–based analysis of the NAD^+ metabolic pathways revealed a decrease of downstream metabolites nicotinamide, 1-methylnicotinamide. and nicotinamide *N*-oxide in the *Ppdpf* KO kidneys, while upstream metabolites tryptophan and quinolinic acid displayed comparable levels to WTs (Fig. 4I). Collectively, these data suggest that *Ppdpf* plays a pivotal role in cellular biosynthesis of NAD^+.

PPDPF deficiency inhibits the functions of NMNATs

To gain further insights into how *Ppdpf* modulates cellular NAD^+ levels, we analyzed its subcellular localization using immunofluorescent staining. The results showed that PPDPF colocalized with mitochondrial markers ATP5A1, HSP60, and TOMM20 (Fig. 5A). In addition, PPDPF was also found in the nuclear fraction as well as cytoplasmic fractions without nucleus according to Western blots of different cellular fractions (Fig. 5B). Furthermore, the subcellular localization predictor (CELLO) predictive system (*37*, *38*) consistently predicted the subcellular localization of PPDPF in the nucleus, mitochondria, and cytoplasmic compartments (table S1). These findings suggest that the functional role of PPDPF extends beyond mitochondria and may have a crucial impact on maintaining cellular NAD^+ homeostasis.

Consistent with this notion, we observed a similar expression pattern between PPDPF and NMNATs. Both proteins showed puncta in the nucleus and filaments in the cytoplasm and mitochondria (fig. S9A), aligning with previous findings that NMNAT1 is predominantly enriched in the nucleus, NMNAT2 mainly localizes to the cytosol, and NMNAT3 is widely expressed in mitochondria (*39*). Given that NMNATs convert NMN into NAD^+ enzymatically (Fig. 5C), we hypothesized that PPDPF might regulate cellular NAD^+ levels through NMNATs. To test this hypothesis, HK2 cells and primary cells were treated with NMN for 4 hours. The data indicated an increase in cellular NAD^+ levels in control cells, but no significant changes were observed in single guide RNA (sgRNA)–treated HK2 cells and *Ppdpf* KO cells (Fig. 5, D and E). In addition, live-cell imaging using the SoNar probe revealed a continuous reduction of NAD^+ levels in *Ppdpf* KO cells after a 4- and 12-hour administration of NMN (Fig. 5, F and G). These findings suggest that *Ppdpf* deficiency disrupts the synthesis of NAD^+ from NMN.

To investigate the modulation of NMNATs expression by *Ppdpf*, we examined RNA and protein levels of NMNATs. However, no significant changes in NMNATs were observed between control and *Ppdpf* KO tissues, *PPDPF* knockdown, or *PPDPF* overexpressing cells (fig. S9, B and C). In contrast, primary cells from *Ppdpf* KO mice showed a decrease in enzymatic activity of NMNATs (Fig. 5H). Thus, we propose that PPDPF physically interacts with NMNATs to regulate their enzymatic activities during NAD^+ synthesis. To test this hypothesis, we overexpressed FLAG-PPDPF and hemagglutinin (HA)–NMNATs in HEK293T cells and performed coimmunoprecipitation (co-IP), which revealed a physical interaction between PPDPF and NMNATs (fig. S9, D and E). Immunofluorescent staining further showed the nuclear colocalization of PPDPF with NMNAT1, cytoplasmic colocalization with NMNAT2, and mitochondrial colocalization with NMNAT3 in HK2 cells (Fig. 5I). Co-IP using anti-NMNATs antibodies and PPDPF antibody confirmed the direct interaction between endogenous PPDPF and all three NMNAT subunits, NMNAT1, NMNAT2, and NMNAT3 (fig. S9F). As a complementary approach to demonstrate the physical interaction between these two proteins, we used an imaging-based proximity ligation assay (PLA) to investigate the spatial proximity of PPDPF and NMNATs. Notably, PLA fluorescent puncta were observed at the interface of PPDPF and NMNATs (Fig. 5, J and K). These collective findings demonstrated that PPDPF physically binds and influences the activities of NMNATs, thereby facilitating the conversion of NMN into NAD^+.

PPDPF modulates the activities of NMNATs through its thiol-disulfide oxidoreductase motif

Previous studies have shown that PPDPF is responsible for NAD^+ synthesis through NMNATs, but the regulatory mechanisms remain unclear. AlphaFold modeling (*40*) indicated few secondary structures in PPDPF (fig. S10A), indicating an improbable direct binding between NAD^+ and PPDPF due to the requirement of a higher secondary fold for NAD^+ binding (*41*). Nevertheless, structural prediction with Phyre2 (*42*) suggested a high confidence for oxidoreductase activity in PPDPF (fig. S10B). Mitochondrial proteomics of WT and *Ppdpf* KO kidneys further showed an abundance of proteins associated with oxidoreductase activity (fig. S10, C and D). Further analysis on the amino acid sequences revealed two cysteines at positions 30 and 35 (Cys30 and Cys35), separated by four other residues. This suggests that PPDPF may function as a disulfide oxidoreductase, as it contains an active disulfide center (CxxxxC) commonly found in pyridine nucleotide disulfide oxidoreductases (Fig. 6A) (*43*).

To determine whether the disulfide bonds in PPDPF were functional or structural, a redox potential assay was performed using 3-(*N*-maleimidopropionyl)-biocytin (MPB) labeling (*44*). The results showed that band intensity increased with a more reducing redox environment (Fig. 6B), indicating a gradual reduction of disulfide bonds and an increase in available free cysteine thiols for MPB labeling. The redox characteristics of PPDPF were further confirmed by constructing two single mutants (C30S and C35S), where the N-terminal active cysteine residue was replaced with serine. All mutants were expressed in *Escherichia coli* and purified, and their activities were compared to those of WT PPDPF protein in disulfide reductase assays. In the insulin reductase assay, the candidate protein cleaves the bridging disulfide bonds of insulin, causing β chain aggregation (*45*). As expected, the WT PPDPF exhibited higher activity compared to the C30S and C35S mutants (Fig. 6C). In addition, we

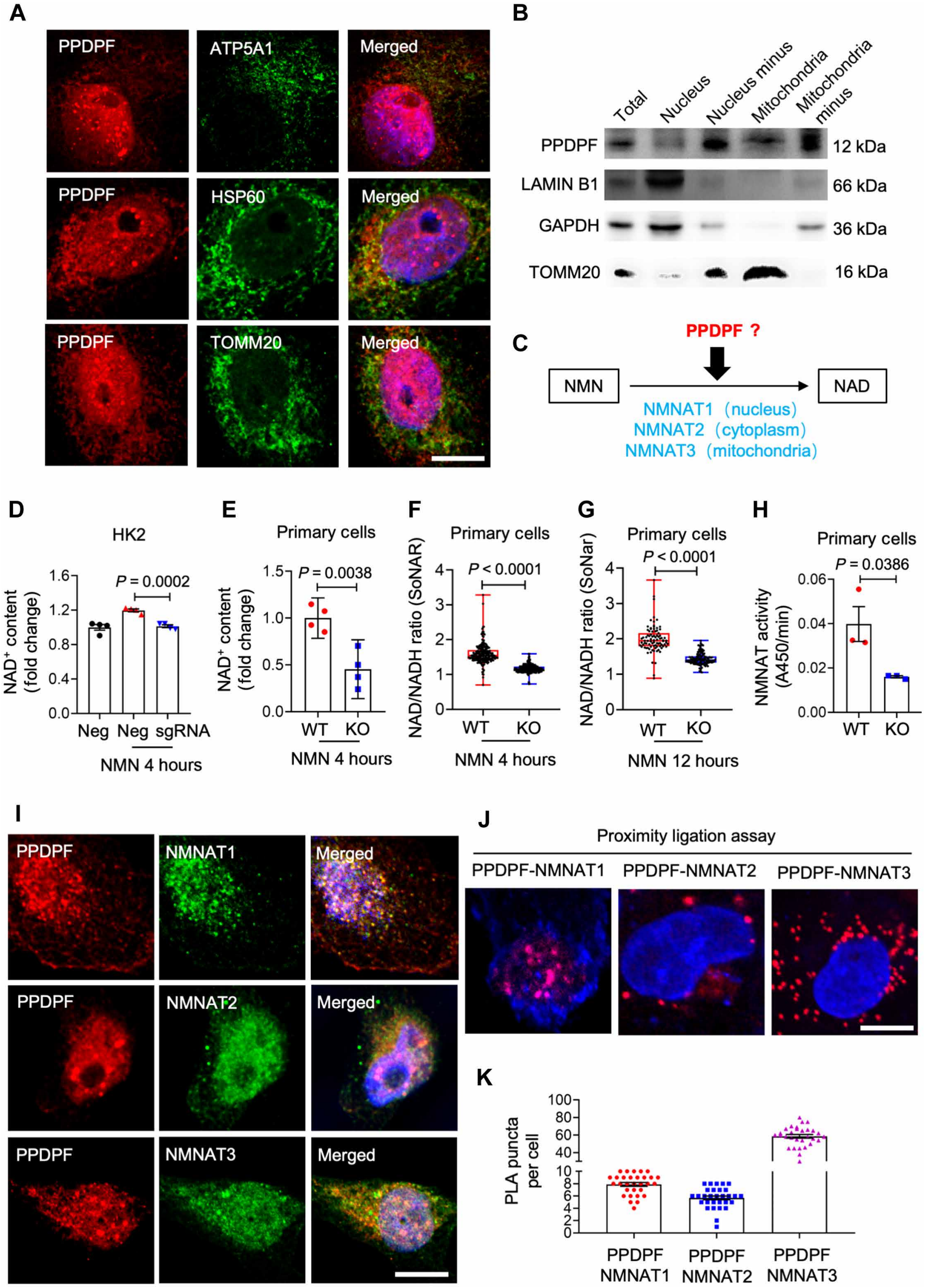

Fig. 5. PPDPF deficiency inhibits NAD$^+$ synthesis through NMNATs. (**A**) Representative images of double staining of PPDPF and mitochondrial markers ATP5A1, HSP60, or TOMM20 in HK2 cells. Scale bar, 10 μm. (**B**) Western blots of subcellular fractions of HK2 cells stained with PPDPF, the mitochondrial antibody TOMM20, and the nuclear antibody LAMIN B1. GAPDH was used as internal control. (**C**) Schematic diagram of PPDPF engages in the synthesis of NAD$^+$ from NMN. (**D**) NAD$^+$ content of sham and sgRNA-targeted HK2 cells following PBS or NMN treatment. (**E**) NAD$^+$ content of primary cells isolated from WT and *Ppdpf* KO kidney following NMN treatment. (**F**) NAD/NADH ratio of primary cells isolated from WT and *Ppdpf* KO mice, treated with NMN for 4 hours and measured with SoNar biosensor. (**G**) NAD/NADH ratio of primary cells isolated from WT and *Ppdpf* KO mice, treated with NMN for 12 hours and measured with SoNar biosensor. (**H**) NMNAT activity of primary cells isolated from WT and *Ppdpf* KO kidney. A450, absorbance at 450 nm. (**I**) Representative double staining of PPDPF with NMNAT1, NMNAT2, or NMNAT3 in HK2 cells. (**J**) Representative images of PLA (red). (**K**) Quantifications of PLA. Scale bar, 10 μm. P value was calculated by two-tailed t test and one-way analysis of variance (ANOVA). $P < 0.05$ is statistically significant. Data are represented as mean ± SEM. (D) $n = 4$ for each group. (E) $n = 4$, WT; $n = 4$, KO. (F) $n = 230$, WT; $n = 209$, KO. (G) $n = 87$, WT; $n = 119$, KO. (H) $n = 3$, WT; $n = 3$, KO. (J) $n = 4$ for each group.

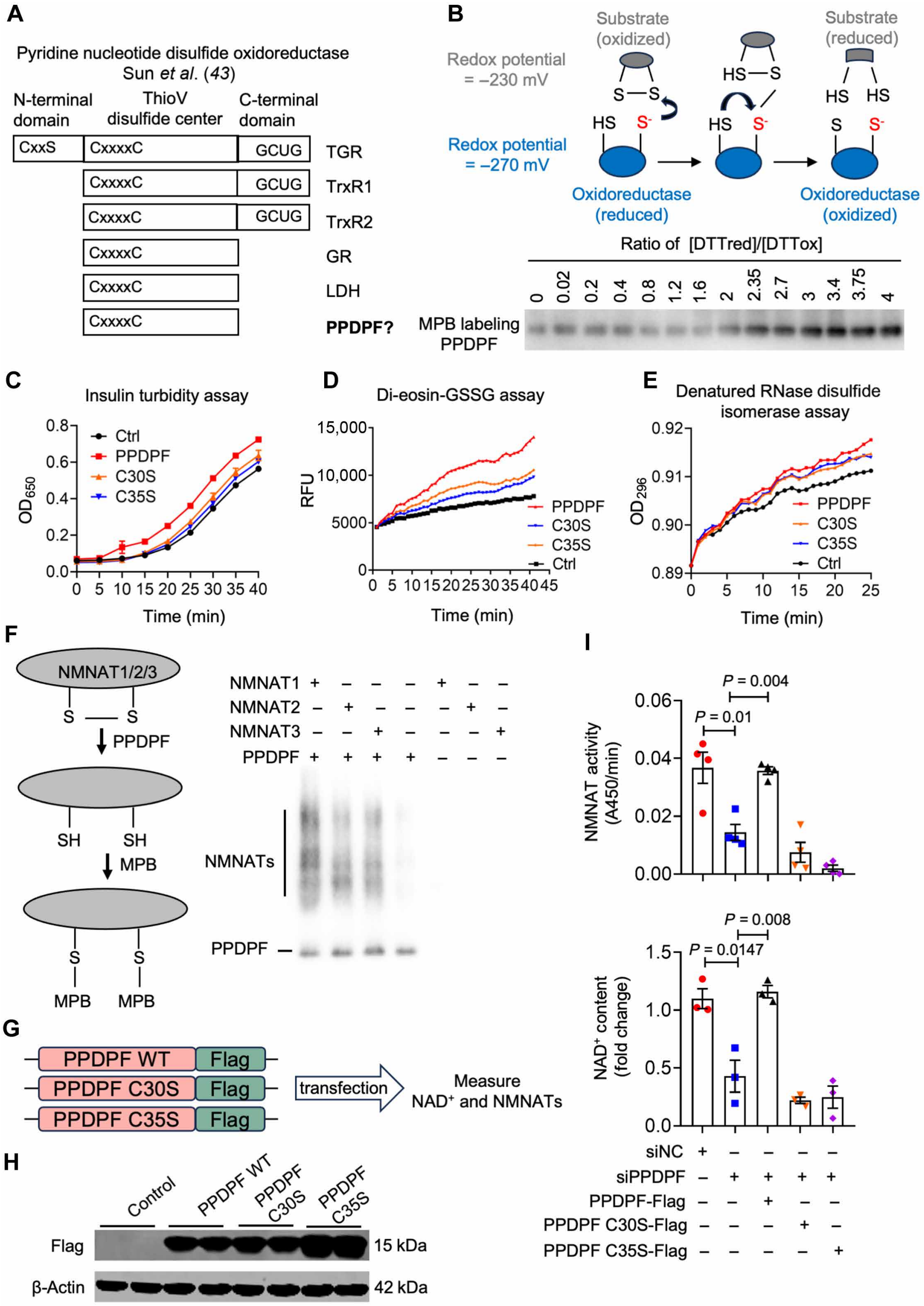

Fig. 6. PPDPF functions as a thiol-disulfide oxidoreductase. (**A**) Schematic representation of the domain organization of TGR, TR1, TR3, GR, LDH, and PPDPF. These six proteins have active disulfide center (the CxxxxC motif; two cysteines separated by four other residues) of the pyridine nucleotide disulfide oxidoreductase family. TGR, thioredoxin (Trx) and GSSG reductase; TrxR1, cytosolic Trx reductase; TrxR2, mitochondrial Trx reductase; GR, GSSG reductase; LDH, lactate dehydrogenase. (**B**) Determination of the redox potential of recombinant human PPDPF by subjecting it to increasing dithiothreitol (DTT) concentrations. The band intensity increases as the redox environment becomes more reducing. This indicates that the disulfide bond is gradually being reduced and resulting in an increase in free cysteine thiols for MPB labeling. (**C**) Optical density readout of an insulin turbidity assay. (**D**) Readout of a di-eosin-GSSG assay using purified proteins. RFU, relative fluorescence unit. (**E**) Readout of an PPDPF RNase disulfide isomerase assay. (**F**) Left: Representation workflow of MPB labeling. PPDPF reduces disulfide bonds, exposing free thiol groups within NMNATs. The free thiols are labeled with MPB, and the proteins are separated by SDS–polyacrylamide gel electrophoresis. Right: Western blot of MPB-labeled NMNATs in the presence of PPDPF. (**G**) Schematic representation of the transfection of PPDPF WT, C30S, and C35S constructs into HEK293T followed by quantifications of NAD$^+$ levels and NMNAT activity. (**H**) Western blots of PPDPF-WT, PPDPF-C30S, and PPDPF-C35S overexpression in HEK293T cells. (**I**) Quantifications of NMNAT activity (top) and NAD$^+$ content (bottom) in cells transfected with indicated constructs. *P* value was calculated by one-way ANOVA. $P < 0.05$ is statistically significant. Data are represented as mean ± SEM. (C to E) $n = 2$ for each group. (H) $n = 2$ for each group. (I) For NMNAT activity, $n = 4$ for each group. For NAD$^+$ measurement, $n = 4$ for each group. OD$_{650}$, optical density at 650 nm.

conducted a di-eosin oxidized glutathione assay (di-eosin-GSSG), commonly used to measure thiol isomerase activity (*44*). Consistently, WT PPDPF showed higher activity than C30S and C35S mutants in this assay as well (Fig. 6D), indicating that these active sites of PPDPF are responsible for its reductase activity. Furthermore, we performed a denatured ribonuclease (RNase) isomerase assay to determine whether the candidate protein catalyzes intramolecular disulfide interchange in scrambled RNase, leading to restoration of native disulfide pairing and recovery of RNase activity (*44*). The results demonstrated that WT PPDPF efficiently refolded scrambled RNase, while mutants appeared less efficient (Fig. 6E), suggesting that at least one active site is required for its isomerase activity. We conducted an assay using thiol reactive probes to investigate whether NMNATs are substrates of PPDPF. Reduction of disulfide bonds by PPDPF introduces free thiols into NMNATs protein which can be detected by incorporating MPB as a free thiol probe and then detecting it using streptavidin–horseradish peroxidase (HRP) probe (Fig. 6F) (*46*). These results demonstrated that three isoforms of NMNAT could efficiently be labeled with MPB in the presence of PPDPF, confirming them as substrates for PPDPF (Fig. 6F).

Next, we investigated whether the reductase activity of PPDPF is responsible for NAD^+ synthesis in eukaryotic cells. We constructed FLAG-tagged eukaryotic expression vectors of PPDPF with or without C30S and C35S mutations (Fig. 6G). The expression level of PPDPF was unaffected by these mutations (Fig. 6H). Subsequently, we transfected WT, C30S, and C35S mutants of the *PPDPF* vectors into HEK293T cells where *PPDPF* had been knocked down by siRNA and then analyzed cellular NAD^+ and NMNAT activity. As expected, knockdown of *PPDPF* resulted in decreased NMNAT activity and NAD^+ levels, which was rescued only by the WT PPDPF but not mutants (Fig. 5I), indicating that the active central disulfides of PPDPF contribute to NAD^+ biosynthesis.

Ppdpf deficiency exacerbates renal injuries in aged mice

Considering the importance of NAD^+ and mitochondria in kidney pathophysiology (*47*, *48*), we investigated the role of PPDPF in aged mice. To address this, we used 12-month-old WT and *Ppdpf* KO littermates (Fig. 7A), as previous studies have shown that liver-specific KO of *Ppdpf* leads to spontaneous fatty liver in mice at 8 months old (*49*). Our findings revealed elevated levels of serum creatinine, BUN, and cystatin C in *Ppdpf* KO mice compared to WTs at 12 months old (Fig. 7, B to D). However, urine albumin and electrolyte levels were similar between WT and KO mice (Fig. 7E and fig. S11A). Histological analysis using hematoxylin and eosin (H&E) and Masson staining showed severe tubular dilation and immune cell infiltration in the kidneys of *Ppdpf* KO mice at 12 months old, while those from WT mice appeared healthier (Fig. 7, F and G). In addition, transcript levels of *Col1a1*, *Col3a1*, and *Vimentin*, as well as the protein levels of vimentin, KIM1, and alpha smooth muscle actin (αSMA), were significantly increased in *Ppdpf* KO mice compared to their WT littermates at 12 months old (Fig. 7, H to J). Consistently, cellular NAD^+ levels were lower in aged *Ppdpf* KO mice than those observed in WTs (Fig. 7K). These findings suggest that *Ppdpf* deficiency accelerated spontaneous kidney injuries.

Ppdpf deficiency exacerbates renal injury in mouse models of cisplatin- and UUO-induced CKD

Then, we examined the susceptibility of *Ppdpf* KO mice to chemical- and obstruction-induced CKD. Eight-week-old male mice were given a low dose of cisplatin via intraperitoneal injection and euthanized 4 weeks later (Fig. 8A), mimicking the nephrotoxicity observed in patients with cancer treated with cisplatin chemotherapy (*50*–*52*). Cisplatin-injected *Ppdpf* KO mice showed higher serum creatinine levels compared to the control group (Fig. 8B), while the urine albumin and electrolyte levels in KO mice after cisplatin treatment were similar to those in WTs (Fig. 8C and fig. S11B). After 1 month of cisplatin injection, *Ppdpf* KO mice displayed more severe histological changes such as loss of PT brush border, tubular dilation, cast formation, and increased collagen accumulation compared to WT mice (Fig. 8, D and E). Consistently, qPCR and Western blot analysis revealed elevated expression levels of fibrosis markers including Col3a1, vimentin, fibronectin, and αSMA in cisplatin-treated *Ppdpf* KO mice (Fig. 8, F and G). Moreover, increased expression levels of DRP1 confirmed mitochondrial damage in *Ppdpf* deficient kidneys following cisplatin treatment (Fig. 8G). In line with these findings, we observed a notable reduction in NAD^+ levels within cisplatin-treated *Ppdpf* KO kidneys compared to WTs (Fig. 8H).

To further validate the impact of *Ppdpf* deficiency on healthy PT clusters, we performed scRNA-seq on WT and *Ppdpf* KO mice with UUO surgery (fig. S12A). The scRNA-seq of WT, *Ppdpf* KO, WT-UUO, and *Ppdpf* KO-UUO kidneys revealed a significant decrease in the proportion of the healthy PT subgroup in *Ppdpf* KO compared to WT (12.85% versus 53.83%) (fig. S12, B to G), further confirming the essential roles of *Ppdpf* in preserving PT cells against injury. These data suggest that *Ppdpf* KO exacerbated renal injuries in cisplatin- and UUO-induced CKD by damaging mitochondria and reducing healthy PT subclusters.

NAD^+ but not NMN ameliorated renal injury in the diseased mice

To investigate the modulation of NAD^+ conversion by *Ppdpf* during disease progression, 8-week-old male WT and *Ppdpf* KO mice were treated with NAD^+ or NMN. They were then intraperitoneally administered FA to induce kidney fibrosis (Fig. 9A). As expected, NAD^+ supplement effectively restored serum creatinine levels in FA-treated *Ppdpf* KO mice, while NMN supplement did not exhibit the same effect (Fig. 9B). Consistently, H&E, Masson, or Sirus red staining also showed that NAD^+, but not NMN, effectively reduced tubule dilation and collagen deposition in the *Ppdpf* KO kidneys (Fig. 9, C and D, and fig. S13). In addition, qPCR and Western blot analysis revealed a reduction in fibrotic markers like *Fibronectin* and *Col3a1* in NAD^+ pretreated *Ppdpf* KO mice (Fig. 9, E and F). However, administration of NMN did not effectively alleviate renal injury induced by FA in *Ppdpf* KO mice (Fig. 9F).

To investigate the interventional effect of NAD^+ in *Ppdpf* KO mice, which has notable clinical implications, we administered NAD^+ 1 day after FA administration (fig. S14A), based on our data indicating an up-regulation of PPDPF 1 day following injury. Supplementation with NAD^+ after FA effectively restored serum BUN levels in FA-treated *Ppdpf* KO mice as well (fig. S14B). Histological analysis using H&E and Sirus red staining demonstrated that NAD^+ supplementation reduced tubule dilation and collagen deposition in *Ppdpf* KO kidneys (fig. S14, C and D). In addition, qPCR analysis revealed a decrease in fibrotic markers such as *Fibronectin* and *Col3a1* in NAD^+-treated *Ppdpf* KO mice (fig. S14E), and immunohistochemistry analyses showed that supplementation with NAD^+ after FA reduced the expression of COL3A1 and ACTA2 in *Ppdpf* KO kidneys (fig. S14F). These findings suggest that early-stage

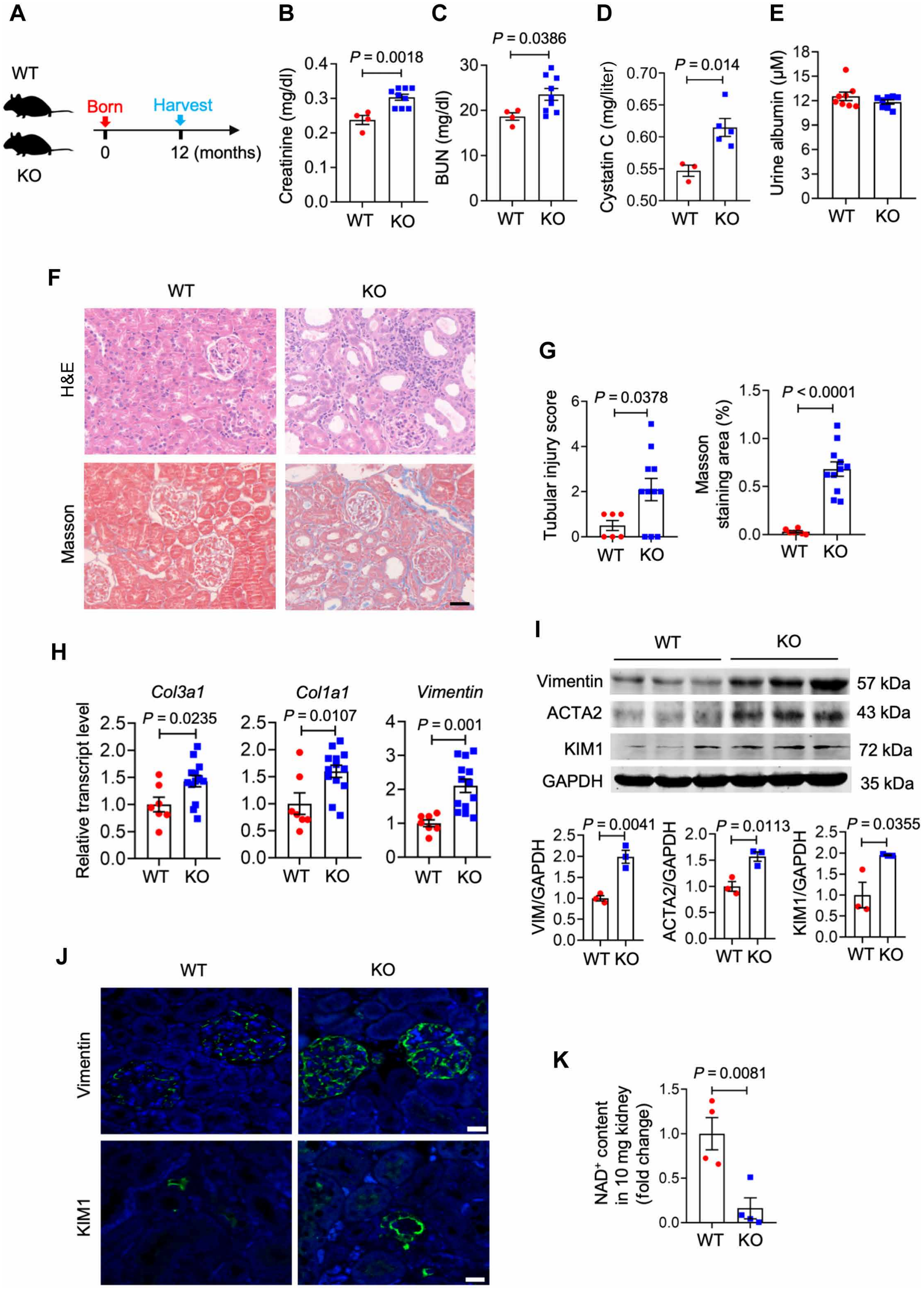

Fig. 7. *Ppdpf* deficiency exacerbates renal injury in aged mice. (**A**) Scheme of the experimental process. Kidneys, serum, and urine were harvested at the age of 12 months. (**B**) Serum creatinine levels in WT and *Ppdpf* KO mice at 12 months old. (**C**) Serum BUN levels in WT and *Ppdpf* KO mice at 12 months old. (**D**) Serum cystatin C levels in WT and *Ppdpf* KO mice at 12 months old. (**E**) Urine albumin levels in WT and *Ppdpf* KO mice at 12 months old. (**F**) Representative images of H&E- and Masson-stained kidney sections from WT and *Ppdpf* KO mice at 12 months old. Scale bar, 20 μm. (**G**) Quantification of tubular injury score and Masson staining area from (F). (**H**) Relative mRNA levels of fibrosis markers *Col3a1*, *Col1a1*, and *Vimentin* in kidneys of WT and *Ppdpf* KO mice at 12 months old. (**I**) Western blots and quantifications of vimentin, ACTA2, and KIM1 in kidneys of WT and *Ppdpf* KO mice at 12 months old. (**J**) Representative images of vimentin and KIM1 staining in kidney sections from WT and *Ppdpf* KO mice at 12 months old. Scale bars, 20 μm. (**K**) NAD$^+$ content of whole kidney lysates of WT and *Ppdpf* KO mice at 12 months old. *P* value was calculated by two-tailed *t* test. $P < 0.05$ is statistically significant. Data are represented as mean ± SEM. (B and C) $n = 4$, WT; $n = 9$, KO. (D) $n = 3$, WT; $n = 5$, KO. (E) $n = 8$, WT; n = 8, KO. (F) $n = 6$, WT; $n = 11$, KO. (H) $n = 7$, WT; $n = 13$, KO. (H) $n = 3$, WT; $n = 3$, KO. (K) $n = 4$, WT; $n = 4$, KO.

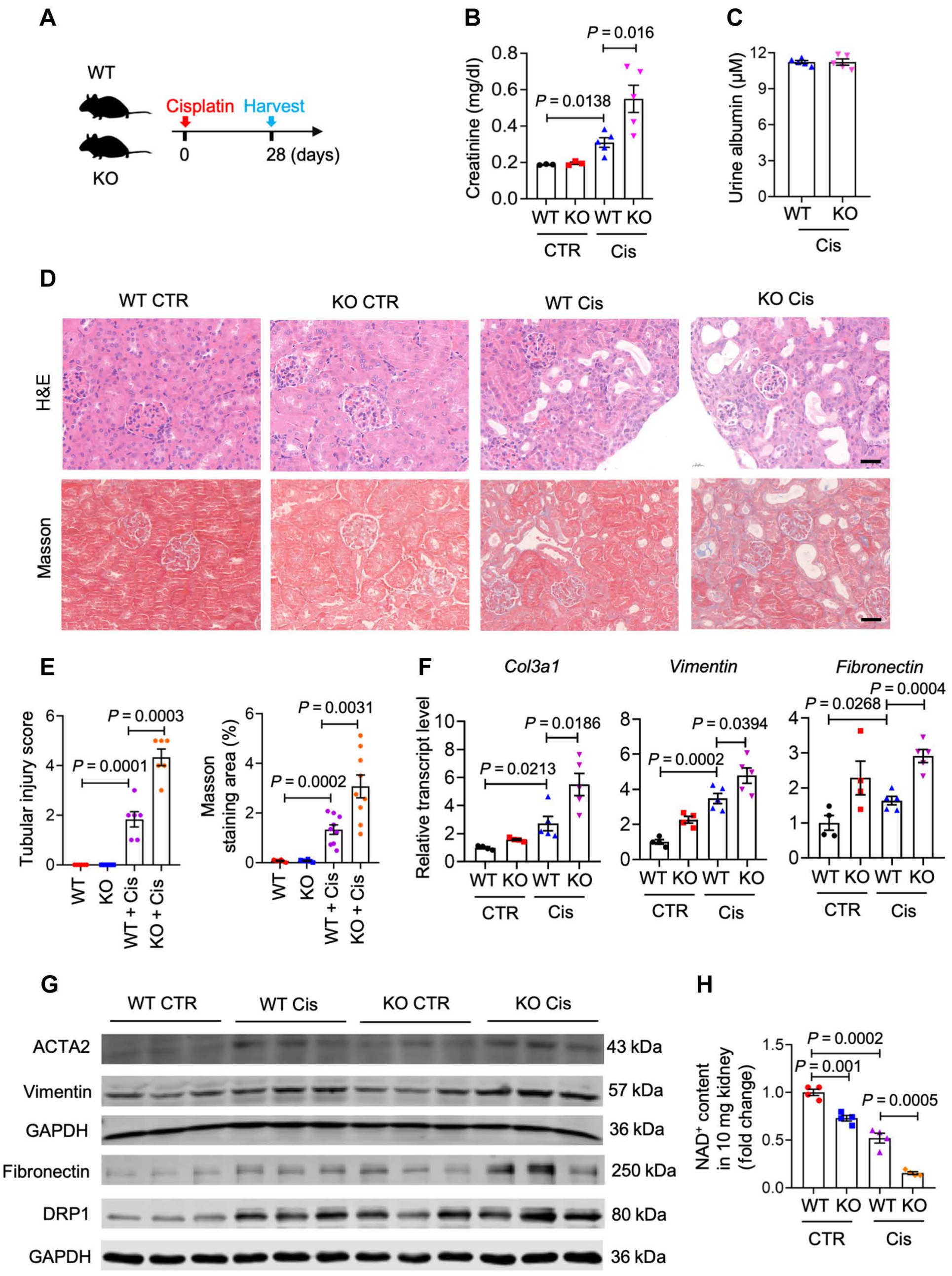

Fig. 8. *Ppdpf* deficiency exacerbates renal injury in the long-term cisplatin model. (**A**) Scheme of the experimental approach. Eight-week-old male mice were intraperitoneally injected with cisplatin (Cis; 7 mg/kg) and euthanized after 28 days. (**B**) Serum creatinine levels of WT and *Ppdpf* KO mice with or without cisplatin treatment. (**C**) Urine albumin levels in WT and *Ppdpf* KO mice with cisplatin treatment. (**D**) Representative images of H&E- and Masson-stained kidney sections from WT and *Ppdpf* KO mice following saline or cisplatin injection. Scale bars, 20 μm. (**E**) Quantification of tubular injury score and Masson staining area from (D). (**F**) The relative expression of fibrosis markers *Col3a1*, *Fibronectin*, and *Vimentin* in control or cisplatin-treated WT and *Ppdpf* KO mice. (**G**) Western blots of fibrosis markers ACTA2, vimentin, fibronectin, and mitochondrial marker DRP1 in WT and *Ppdpf* KO mice with or without cisplatin treatment. (**H**) NAD^+ content of whole kidney lysates of WT and *Ppdpf* KO mice with or without cisplatin treatment. *P* value was calculated by one-way ANOVA. $P < 0.05$ is statistically significant. Data are represented as mean ± SEM. (B) $n = 4$, WT CTR; $n = 3$, KO CTR; $n = 5$, WT Cis; $n = 5$, KO Cis. (C) $n = 5$, WT Cis; $n = 5$, KO Cis. (E) $n = 3$, WT CTR; $n = 3$, KO CTR; $n = 6$, WT Cis; $n = 6$, KO Cis. (F) $n = 4$, WT CTR; $n = 4$, KO CTR; $n = 5$, WT Cis; $n = 5$, KO Cis. (G) $n = 3$, WT CTR; $n = 3$, KO CTR; $n = 3$, WT Cis; $n = 3$, KO Cis. (H) $n = 4$, WT CTR; $n = 4$, KO CTR; $n = 4$, WT Cis; $n = 4$, KO Cis.

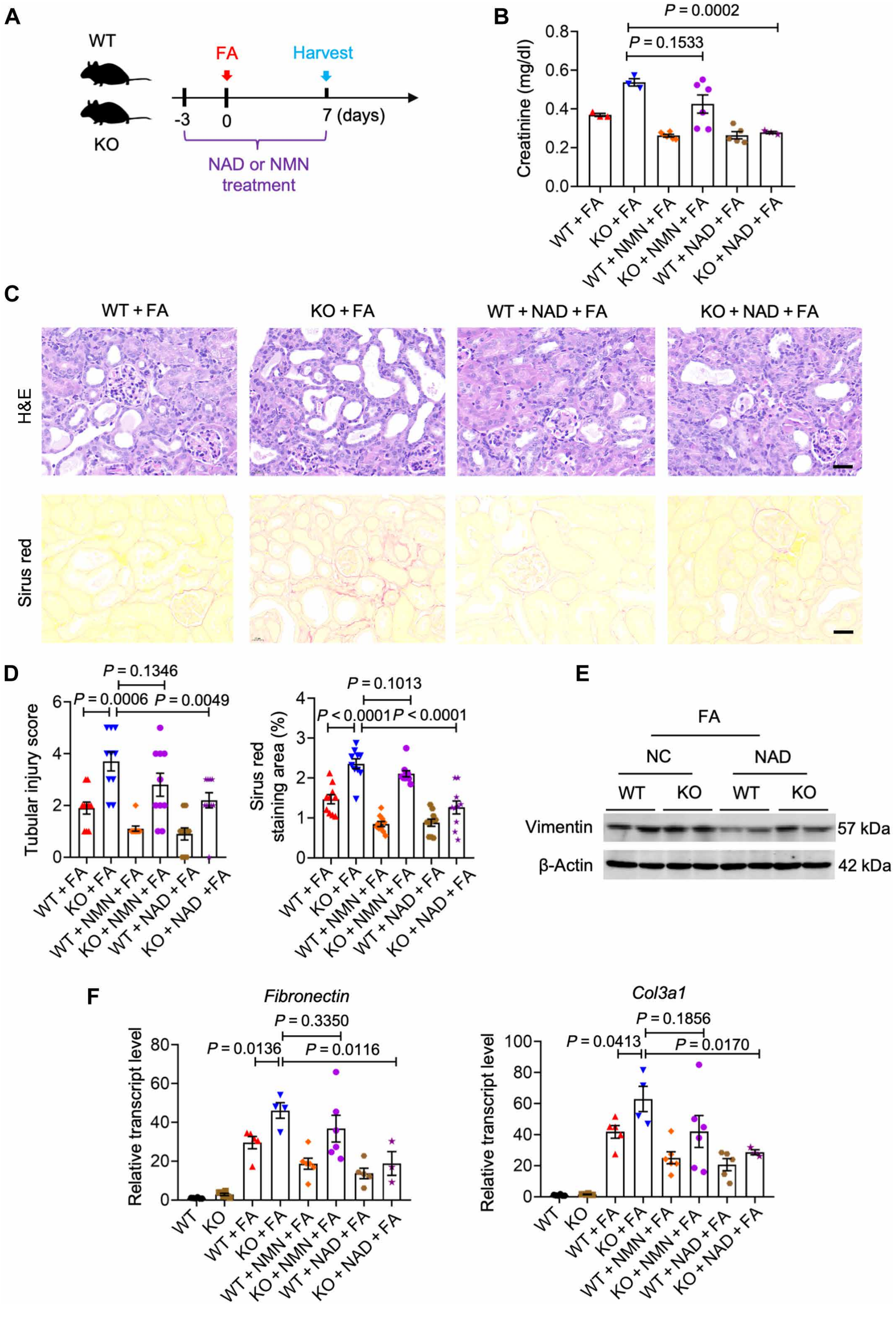

Fig. 9. NAD$^+$ but not NMN alleviates the renal injuries in *Ppdpf* KO mice with FA treatment. (**A**) Scheme of the experimental approach. Eight-week-old male mice were intraperitoneally injected with NAD$^+$ (3 mg/g) or NMN (500 mg/kg). FA (250 mg/kg) was injected 3 days later, and mice were then euthanized after 7 days. (**B**) Serum creatinine levels of WT and *Ppdpf* KO mice with or without FA, NAD$^+$ or NMN treatment. (**C**) Representative images of H&E- and Sirus red–stained kidney sections from WT and *Ppdpf* KO mice following FA and NAD injection. Scale bar, 20 μm. (**D**) Quantifications of tubular injury score and Sirus red staining area in the kidneys of WT and *Ppdpf* KO mice with or without FA, NMN, or NAD$^+$ administration. (**E**) Western blots of vimentin in kidneys of WT and *Ppdpf* KO mice with or without FA and NAD$^+$ treatment. (**F**) The relative expression of fibrosis markers *Fibronectin* and *Col3a1* in kidneys of WT and *Ppdpf* KO mice with or without FA, NMN, or NAD$^+$ administration. *P* value was calculated by one-way ANOVA. $P < 0.05$ is statistically significant. Data are represented as mean ± SEM. (B) $n = 3$, WT + FA; $n = 3$, KO + FA; $n = 6$, WT + NMN + FA; $n = 6$, KO + NMN + FA; $n = 5$, WT + NAD + FA; $n = 3$, KO + NAD + FA. (D) $n = 10$ for each group. (E) $n = 2$ for each group. (F) $n = 4$, WT; $n = 4$, KO; $n = 3$, WT + FA; $n = 3$, KO + FA; $n = 6$, WT + NMN + FA; $n = 6$, KO + NMN + FA; $n = 5$, WT + NAD + FA; $n = 3$, KO + NAD + FA.

administration of NAD^+ can also alleviate renal injuries. Overall, our results highlight the crucial protective role of *Ppdpf* in modulating cellular NAD^+ levels to mitigate renal injuries.

Ppdpf **overexpression protected kidney from FA-induced renal injuries**

In addition to loss of function, we performed a rescue approach by injecting adeno-associated virus serotype 9 encoding *Ppdpf* (AAV9-PPDPF) and AAV9-Ctrl into the renal cortex of 8-week-old male mice as previously described (*53*, *54*). Subsequently, FA was injected to induce kidney injuries in mice (Fig. 10A). After a 4-week injection of AAV9-PPDPF, transcript levels of *Ppdpf* were significantly increased in the kidneys, along with an increase in protein expression levels tagged by the FLAG and PPDPF antibodies (Fig. 10, B and C). In addition, immunofluorescent staining revealed enhanced PPDPF signals in the LTL-positive tubule of AAV9-PPDPF kidneys compared to AAV9-Ctrl (fig. S15). The up-regulation of PPDPF in PTs was further investigated by isolating LTL-positive cells and subjecting them to the analysis of PPDPF protein levels, which showed a remarkable increase (Fig. 10D). Moreover, overexpression of *Ppdpf* improved tubular dilation and collagen deposition caused by FA (Fig. 10, E and F). qPCR and immunohistochemistry analyses showed that *Ppdpf* overexpression reduced the expression of fibrosis and renal injury markers in kidneys (Fig. 10, G and H). Furthermore, NAD^+ levels and NMNAT activity consistently increased in kidneys with *Ppdpf* overexpression (Fig. 10, I and J), indicating that PPDPF contributes to NMNAT activity and NAD^+ synthesis in vivo. These findings suggest that *Ppdpf* overexpression exhibits a protective effect against renal injuries through synthesis of NAD^+.

DISCUSSION

Here, we found that metabolic dysfunction in PT cells is a key feature of early-stage kidney injuries. The eGFR GWAS target gene *PPDPF* is up-regulated in healthy PT subclusters in humans and animals as a compensatory response. *Ppdpf* deficiency results in mitochondrial damage and reduces NAD^+ levels in HEK293T, HK2, and primary cells. Mechanistically, PPDPF regulates NMNAT activity through its oxidoreductase domain. Consistently, genetic ablation of *Ppdpf* leads to spontaneous kidney injuries in aged mice and exhibits more severe kidney fibrosis in chemical- and obstruction-induced mouse CKD models, which can be attenuated by overexpressing PPDPF or supplementing NAD^+ but not NMN.

First, comprehensive transcriptomic analyses of kidney tissues have been conducted to define the molecular hallmarks of CKD in both human samples and mouse models (*55*–*57*), revealing a correlation between numerous transcripts and kidney fibrosis. However, most studies primarily focus on genetic functions during the irreversible late stages of CKD. Kidney epithelial cells rapidly sense even minor changes in fluid due to their role in reabsorbing 99% of water and ions/nutrients (*58*). For instance, the expression of mechanosensitive Piezo1 increases within 30 min after UUO surgery (*59*). Our study aligns with previous findings that among all cell types in kidneys, PT cells exhibit notable responses at the early stages of UUO. Therefore, emphasizing the early stages of kidney fibrosis could help identify pivotal molecules or pathways driving CKD progression.

Second, renal tubular epithelial cells contain abundant mitochondria, which is second only to that in cardiomyocytes. Mitochondria continuously produce adenosine triphosphate (ATP) to maintain the reabsorption function of renal tubules. NAD^+ serves as a mitochondrial "fuel" for the respiratory chain and regulates cellular energy transduction through ATP production (*60*). Dysregulation of NAD^+ homeostasis has been observed in both human and animal models of kidney injuries (*48*, *61*–*63*). On one hand, administration of NAD^+ precursors, such as nicotinamide, nicotinamide riboside, and NMN, protects against kidney injury in rodents (*62*, *64*). However, few studies have shown protective effects from the 25 clinical trials on nicotinamide riboside supplements (*65*). On the other hand, NMN supplementation has shown promising potential for boosting NAD^+ levels in rodents (*66*–*68*). However, further mechanism study is needed to understand the conversion of NMN into NAD^+ before expanding its applications in CKD and other diseases due to limited clinical trials on NMN (*69*). In addition, differences in NAD^+ synthesis and metabolism between mice and humans may be attributed to distinct genetic backgrounds or bioavailability of NAD^+ precursors across species which require further investigation. PPDPF was reported to be located within mitochondria via the mitochondrial high-confidence proteome assay (*70*), suggesting that its primary function is closely related to metabolism. Accordingly, our study identified PPDPF as an oxidoreductase that regulates NMNAT activity and NAD^+ synthesis, maintaining mitochondrial homeostasis in response to kidney injuries. Our study revealed that PPDPF showed a compensatory increase in the early stages of CKD while gradually decreased as the disease progressed, and only NAD^+ but not NMN exhibited protective effects on mice with CKD. These findings further highlighted the importance of PPDPF in the biosynthesis of NAD^+ in vivo and could be a potential therapeutic intervention for patients with kidney diseases. Because of its high metabolic activity, the kidney has been emerged as an intriguing system for studying NAD^+ biology. Considering the ubiquitous widespread presence of NAD^+ metabolism in cellular homeostasis, insights gained from kidney may provide perspectives applicable to other organs.

Last, the high failure rates and substantial costs associated with developing new drugs in clinical trials can largely be attributed to unforeseen adverse side effects (*71*). Recent studies indicate that tissue-specific genetic features can predict drug side effects in clinical trials (*72*). Specifically, human genetic data can be used to predict drug safety profiles by targeting genes supported by genome-wide association loci for related phenotypes, as drugs causing side effects are more likely to do so (*73*). For instance, the adenosine triphosphatase Na^+/K^+ transporting subunit alpha 1 (*ATP1A1*) gene, a target for heart failure, shows an eQTL signal in both colonic and esophageal tissues. Clinical trial results have demonstrated that drugs targeting *ATP1A1*, such as digoxin, induce gastrointestinal adverse effects such as nausea, vomiting, and diarrhea (*74*, *75*). In our study, we have shown that PPDPF is a risk gene for CKD based on GWAS data. In addition, we have elucidated its role in maintaining PT integrity in kidneys. However, previous studies have reported that PPDPF inhibits cancer development such as pancreatic ductal adenocarcinomas (*76*) and lung adenocarcinoma development (*17*). The differential effects of PPDPF between cancerous and nontumor tissues suggest potential nephrotoxicity when targeting PPDPF for cancer treatment. Our findings not only contribute to further analysis of NMN's clinical efficacy but also emphasize considering nephrotoxic side effects when developing and using anticancer drugs targeting PPDPF.

MATERIALS AND METHODS

Bulk RNA-seq

Total RNA was extracted using TRIzol reagent (Thermo Fisher Scientific, #15596018) following the manufacturer's procedure. Subsequently, the

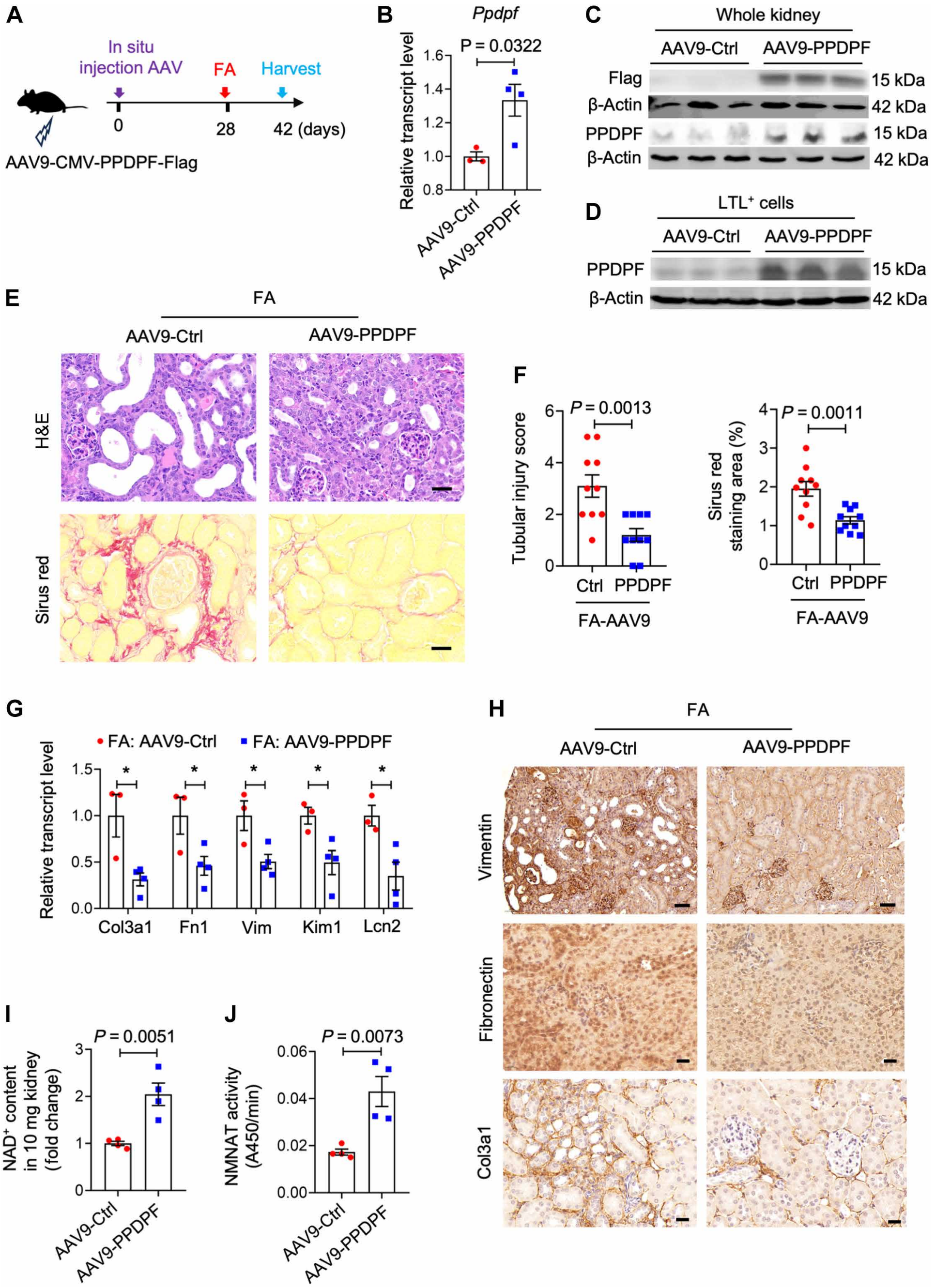

Fig. 10. Overexpression of *Ppdpf* alleviates kidney fibrosis induced by FA administration. (**A**) Schematic diagram of *Ppdpf* overexpression in mice. Eight-week-old male mice were in situ injected with AAV9 encoding *Ppdpf* or scramble. Post–4-week injection, the mice were subjected to FA treatment. (**B**) The relative expression levels of *Ppdpf* in kidneys with AAV9-Ctrl or AAV9-PPDPF injections. (**C**) Western blots of Flag and PPDPF in kidneys with AAV9-Ctrl or AAV9-PPDPF injections. (**D**) Western blots of PPDPF in LTL-positive cells from AAV9-Ctrl or AAV9-PPDPF kidneys. (**E**) Representative images of H&E- and Sirus red–stained kidney sections from AAV9-Ctrl– or AAV9-PPDPF–injected mice following FA administration. Scale bars, 20 μm. (**F**) Quantifications of tubular injury score and Sirus red staining area from (E). (**G**) The relative expression levels of fibrosis markers *Col3a1*, *Vimentin*, and *Fibronectin*, as well as injury markers *Kim1* and *Lcn2* in kidneys of AAV9-Ctrl– or AAV9-PPDPF–injected mice following FA administration. $^*P < 0.05$. (**H**) Representative images of vimentin, fibronectin, and Col3a1 staining on kidney sections from AAV9-Ctrl– or AAV9-PPDPF–injected mice following FA administration. Scale bars, 50 or 20 μm. (**I**) NAD^+ content of whole kidney lysates from AAV9-Ctrl– or AAV9-PPDPF–injected mice. (**J**) NMNAT activity of primary cells isolated from AAV9-Ctrl– or AAV9-PPDPF–injected kidneys. *P* value was calculated by two-tailed *t* test (B, F, I, and J) and two-way ANOVA (G). $P < 0.05$ is statistically significant. Data are represented as mean ± SEM. (B) $n = 3$, AAV9-Ctrl; $n = 4$, AAV9-PPDPF. (C and D) $n = 3$ for each group. (F) $n = 10$ for each group. (G) $n = 3$, FA-AAV9-Ctrl; $n = 4$, FA-AAV9-PPDPF. (I) $n = 4$ for each group.

quantity and purity of the total RNA were assessed using the Bioanalyzer 2100 and the RNA 6000 Nano LabChip Kit (Agilent, CA, USA, 5067-1511). Only high-quality RNA samples with an RNA Integrity Number (RIN) number >7.0 were used for constructing a sequencing library. The Illumina Novaseq 6000 platform by LC Bio Technology Co. Ltd. (Hangzhou, China) was used for sequencing the RNA libraries. Alignment of reads from all samples to either the rat or mouse reference genome was performed using HISAT2 (*77*) software (https://daehwan-kimlab.github.io/hisat2/, version: hisat 2-2.0.4). StringTie and ballgown (*78*) tools were used to estimate expression levels of all transcripts and calculate FPKM (fragment per kilobase of transcript per million mapped reads) values for mRNA abundance analysis. Differential gene expression analysis between two different groups was conducted using DESeq2 software; edgeR was used when comparing two samples instead (*79*). Genes exhibiting a false discovery rate (FDR) parameter below 0.05 and an absolute fold change of ≥2 were considered as DEGs.

Single-cell RNA-seq

Euthanized mice were perfused with chilled 1× phosphate-buffered saline (PBS) through the left ventricle. Kidneys were harvested, minced into approximately 1-mm^3 cubes, and digested using a Multi Tissue dissociation kit (Miltenyi, 130-110-201). The tissue was homogenized using 21G and 26 1/2G syringes. Up to 0.25 g of the tissue was digested with 50 μl of enzyme D, 25 μl of enzyme R, and 6.75 ml of enzyme A in a total volume of RPMI 1640 (1 ml) and incubated for 30 min at 37°C. The reaction was deactivated by adding 10% fetal bovine serum (FBS). Subsequently, the solution was passed through a cell strainer with a pore size of 40 mm. After centrifugation at 400*g* for 5 min, the resulting cell pellet was incubated with red blood cell lysis buffer (1 ml) on ice for 3 min. Cell number and viability were analyzed using Countess Auto Counter (Invitrogen, C10227). This method generated single-cell suspension with more than 80% viability.

The single-cell suspensions were loaded onto a 10× Chromium system following the manufacturer's instructions of the 10× Genomics Chromium Single-Cell 3′ kit (V3). Subsequently, cDNA amplification and library construction steps were carried out according to the standard protocol. For sequencing, libraries were subjected to paired-end multiplexing run on an Illumina sequencing system with a read length of 150 bp. LC-Bio Technology Co. Ltd. (HangZhou, China) performed the sequencing at a minimum depth of 20,000 reads per cell.

The sequencing results were demultiplexed and converted to FASTQ format using Illumina bcl2fastq software (version 2.20). Sample demultiplexing, barcode processing and single-cell 3′ gene counting were performed using the Cell Ranger pipeline (version 3.1.0), with scRNA-seq data aligned to Ensembl genome GRCm38 or mRatBN7.2 reference genome. A total of 120,000 single cells were captured from three healthy rat kidneys, three UUO 1d kidneys, and two UUO 5d kidneys; in addition, a total of 40,000 single cells were captured from one WT kidney, one *Ppdpf* KO kidney, one WT UUO kidney, and one *Ppdpf* KO UUO kidneys using a 10× Genomics Chromium Single Cell 3′ Solution kit. The output from Cell Ranger was imported into Seurat (version 3.1.1) for dimensional reduction analysis and clustering, and further analysis of scRNA-seq data quality control measures included removing genes expressed in less than three cells; setting a cutoff of >500 genes expressed per cell as low expression and <5000 genes expressed per cell as high expression; filtering out unique molecular identifier (UMI) counts less than 500; and ensuring that the percentage of mtDNA-derived gene expression was below <25%.

Seurat R package (version 2.3.4) was used for data quality control, preprocessing, and dimension reduction analysis. After generating the gene cell data matrix, cells of poor quality were excluded on the basis of the criteria of having less than 200 or more than 3000 expressed genes. In addition, genes expressed in fewer than 10 cells as well as mitochondrial genes, ribosomal protein genes, and human leukocyte antigen genes known to induce unwanted batch effects were removed for subsequent analysis. Cells with mitochondrial gene percentages exceeding 50% were also discarded. To normalize the sequencing depth to a total of 10,000 molecules per cell, the data underwent natural logarithm transformation and scaling followed by regression-out of UMI and gene counts. The batch effect was corrected using the "remove Batch Effect" function in edgeR. The expression values after batch correction were exclusively used for PCA, Uniform Manifold Approximation and Projection (UMAP) visualization, and clustering analyses. The original expression values before batch correction were used for downstream analyses such as marker gene identification and differential gene expression analysis. To perform dimension reduction, highly variable genes across single cells were identified using a low cutoff of 0.0125 and a high cutoff of 0.3. PCA was performed using the variable genes as input, and top 20 principal components were used for the initial UMAP projection. Marker genes for each cluster were identified through the Wilcoxon rank-sum test (with default parameters, "bimod": likelihood ratio test) using the Find All Markers function in Seurat. This approach selects marker genes that are expressed in more than 10% of cells within a cluster and have an average log fold change greater than 0.25. A resolution of 0.5 was used for subclustering of the clusters. Differential expression analysis was conducted for every pair of subclusters, with merging occurring when there were fewer than or equal to 15 DEGs (10 differential genes specifically for T lymphocytes) exhibiting an average expression difference greater than one natural logarithm and FDR-corrected *P* value less than 0.01. As a result of this clustering analysis, a total of 35 cell clusters were obtained. Subsequently, PT cell clusters underwent further subclustering.

Targeted metabolomics

The kidney sample (100 mg) was vortexed in 1 ml of cold methanol/acetonitrile/H_2O (2:2:1, v/v/v) and homogenized using an MP Biomedicals FastPrep homogenizer (24 × 2, 6.0 MS, 60 s, twice). Subsequently, the homogenate underwent sonication twice at 4°C followed by centrifugation at 14,000*g* for 20 min. The resulting supernatant was dried using a vacuum centrifuge. For LC-MS analysis, the samples were redissolved in 100 μl of acetonitrile/water (1:1, v/v), thoroughly vortexed again, and then subjected to centrifugation (14,000*g*, 4°C, 15 min). Last, the supernatants were collected for LC-MS/MS analysis using an UHPLC system (1290 Infinity LC, Agilent Technologies) coupled with a quadrupole ion trap (QTRAP) instrument (AB Sciex 5500).

The samples were subjected to hydrophilic interaction liquid chromatography (HILIC) separation using an ACQUITY UPLC BEH Amide column (2.1 mm by 100 mm, 1.7 μm, Waters MS Technologies, Manchester, UK). A mobile phase consisted of A = 15 mM CH_3COONH_4 in water and B = acetonitrile was used. The samples were stored at 4°C in the automatic sampler, while the column temperature was maintained at 45°C throughout the analysis. Gradients were run at a flow rate of 300 μl/min with each sample injected as a 2-μl aliquot. The gradient initiated with 90% B and gradually decreased to 40% within the first 0 to 18 min and then rapidly increased to reach 90% within an additional minute before further increasing to 85% within another minute and maintaining this composition from 18.1 to 23 min. Quality control samples prepared from pooled samples were interspersed after every five regular samples for monitoring method precision and operational stability.

To construct the metabolite MS/MS Analysis [multiple reaction monitoring (MRM)] library, each metabolite standard (100 mg/ml) was initially analyzed in electrospray ionization negative mode via flow injection to obtain the optimal MRM transition parameters. Subsequently, the retention time of each metabolite was determined by individually measuring its corresponding MRM (Q1/Q3) transition on the column. A standard mixture sample (32 STD_mix), containing all 32 metabolites, was measured together with biological samples in every experiment. LC-MS quantification of energy metabolites was achieved with six-point standard curves prepared by diluting succinic acid (D6, 98%, DLM-831-5, Cambridge Isotope laboratories, Inc.) in a relevant matrix matched to the analytical sample for absolute quantification. Data acquisition and processing were performed using Multiquant software.

Animals

The study used male C57BL/6 mice for in vivo experiments. All mice were bred and maintained in specific pathogen–free conditions in the animal facilities of East China Normal University. All animal experiments were reviewed and approved by the Laboratory animal Welfare Ethics Committee of the East China Normal University (ethics approval numbers: ARXM2022106 and m20240901).

The *Ppdpf* mutant mice were generated by coinjection of Cas9 mRNA and sgRNA in the strain of C57BL/6 mice as described previously (*80*). The sgRNA sequences and genotyping primers were listed in table S2.

For the UUO model, 8-week-old male mice underwent ligation of their left ureter and were euthanized on day 1 or day 5, while sham-operated mice were used as controls. For the cisplatin-induced injury model, 8-week-old male WT and *Ppdpf* KO mice received weekly intraperitoneal injections of cisplatin (7 mg/kg) for 4 weeks (*50*). For FA-induced nephropathy mouse models, 8-week-old male WT and *Ppdpf* KO mice received intraperitoneal injections of FA (250 mg/kg) before being euthanized on day 7 (*81*). Mice receiving NAD^+ treatment had a daily intraperitoneal injection (3 mg/g) (*82*) during FA treatment; those receiving NMN treatment had a daily intraperitoneal injection of NMN (500 mg/kg) during FA treatment.

To induce overexpression of PPDPF in kidneys, AAV9-mediated delivery was used. Male C57BL/6J mice aged 8 to 10 weeks were used for this study. Briefly, mice were anesthetized with isoflurane and subsequently injected with 1.5×10^{12} vector genome (vg)/ml AAV9-CMV-PPDPF-3 × FLAG and 1.5×10^{12} vg/ml AAV9 control into five distinct sites (5 μl at each site) within the renal cortex using a glass micropipette.

Serum BUN, creatinine, and cystatin C levels

The levels of serum creatinine and BUN were determined using the BX-3010 Automatic biochemical analyzer, following the instructions provided by the manufacturers. The measurement of serum cystatin C was performed using the cystatin C (mouse) ELISA Kit (Beyotime Biotechnology).

Cell culture

HEK293T cells were cultured in Dulbecco's modified Eagle's medium (DMEM) supplemented with 10% FBS and 1% penicillin-streptomycin at a temperature of 37°C and under a CO_2 concentration of 5%. Meanwhile, HK2 cells were cultured in DMEM/F12 medium containing 10% FBS, epidermal growth factor (EGF; 5 ng/ml; PeproTech, #AF-100-15), 1× insulin-transferrin-selenium supplement (ITS; Gibco, #51500-056), and 1% penicillin-streptomycin (Corning, #30-002-CI) under the same conditions. All cell lines underwent regular mycoplasma testing.

siRNA knockdown

The siRNA targeting human *PPDPF* (RiboBio Co. Ltd.) was resuspended in a 10 mM tris (pH 8.0) buffer at a concentration of 20 μM. Cells were seeded in six-well plates, cultured overnight until they reached 60 to 70% confluency, and subsequently transfected with siRNA at a final concentration of 50 nM using Lipofectamine 3000. Following treatment, cells were incubated for 48 hours before being subjected to experimental procedures.

Cloning and expression

The cDNA sequences of human PPDPF, PPDPF-C30S, and PPDPF-C35S were tagged with a C-terminal 3× FLAG epitope and ligated into the Plv-ER-GFP vector (Addgene, #80069) that was linearized by Xho I and Xba I restriction enzymes. Similarly, the cDNA sequences of human NMNAT1, NMNAT2, and NMNAT3 were tagged with an HA epitope and cloned into the Plv-ER-GFP vector using Xho I and Xba I restriction enzymes. *E. coli* codon–optimized human NMNAT1, NMNAT2, and NMNAT3 were cloned into the pGEX4t-1 vector using Bam HI and Not I restriction endonucleases. In addition, *E. coli* codon–optimized human PPDPF was inserted into pET28a vector using Eco RI and Sal I restriction endonucleases.

Lentivirus production and transduction of cell lines

HEK293T cells were seeded into a 10-cm dish 1 day before transfection. Upon reaching approximately 85% confluency, they were cotransfected with 10 μg of transfer plasmid (lentiCRISPR v2-sgPPDPF), 5 μg of pMD2.G, and 7.5 μg of psPAX2. The viral supernatant was collected at 48 and 72 hours posttransfection. To remove cellular debris, the supernatant was centrifuged at 4000*g* for 10 min at 4°C, filtered through a low-protein binding membrane (0.45-μm pore size, Millipore), and subsequently concentrated by centrifugation at 25,000*g* for 2.5 hours at 4°C.

Generation of stably transfected HK2 cells

The parental HK2 cells were cultured in DMEM/F12 medium supplemented with 10% FBS, EGF (5 ng/ml) from PeproTech (#AF-100-15), ITS (Gibco #51500-056), and penicillin-streptomycin. After 3 days of lentiviral transduction in a 10-cm dish, the transfected HK2 cells were incubated for 2 weeks in complete DMEM/F12 medium containing puromycin at a concentration of 2 μg/ml, with regular replacement of the medium every other day. Cells that stably expressed the transgene were confirmed by immunofluorescence and immunoblot analysis.

LTL^+ cell isolation and cultivation

The kidneys were obtained from male mice aged 3 to 5 weeks. Cells were isolated by digestion with collagenase I (Gibco, #17018-029) at a concentration of 2 mg/ml for 30 min at 37°C with gentle stirring.

Subsequently, the cells were sequentially filtered through mesh sizes of 100, 70, and 40 μm to obtain single cells. After centrifugation, the supernatant was discarded. A working concentration of LTL biotin antibody at 20 μg/ml was added along with 2 ml of magnetic-activated cell sorting (MACS) buffer. The mixture was incubated on ice for 10 to 15 min and then washed with MACS buffer before undergoing another round of centrifugation. Meanwhile, a solution containing beads was prepared by combining 20 μl of beads with 400 μl of MACS buffer. The supernatant of the cells was replaced with the bead solution and incubated on ice for an additional period of time lasting approximately 15 min while gently shaking in between. After a second wash with MACS buffer, the cell suspension was resuspended in 500 μl of buffer and loaded onto the MS column. Following three washes with 500 μl of buffer each time, cells were collected by pushing the plunger into the column. Last, cells were cultured in RPMI 1640 (Sangon Biotech, #E600028) supplemented with 10% FBS (Gibco, #A5256701), EGF (20 ng/ml; PeproTech, #AF-100-15), 1× ITS (Gibco, #51500-056), and 1% penicillin-streptomycin at a temperature of 37°C under 5% CO_2.

Transmission electron microscopy

The mitochondrial structure was examined using standard transmission electron microscopy. Fresh kidney tissue was fixed overnight with a mixture of 2% paraformaldehyde and 2.5% glutaraldehyde, followed by thorough washing, dehydration, and embedding in resin according to established protocols. Subsequently, the embedded samples were analyzed using a transmission electron microscope (Hitachi, Japan).

Western blot

Kidney tissues or cultured cells were lysed in ice-cold lysis buffer [50 mM tris-base (pH 7.4), 150 mM NaCl, 1% Triton X-100, 1% sodium deoxycholate, 0.1% SDS, and a protease inhibitor cocktail (cOmplete Mini; Roche, #11836153001)]. Protein extracts were quantified by the Micro BCA Protein Assay Kit (Thermo Fisher Scientific), resolved by SDS–polyacrylamide gel electrophoresis, and probed with the following antibodies: PPDPF (Proteintech, #19912-1-AP), NDUFB9 (Proteintech, #15572-1-AP), NDUFS3 (Proteintech, #15066-1-AP), SDHA (Proteintech, #14865-1-AP), SDHB (Proteintech, #10620-1-AP), LAMIN B1 (Proteintech, #66095-1-Ig), TOMM20 (Proteintech, #66777-1-Ig), Flag (Proteintech, #66008-3-Ig), vimentin (Proteintech, #10366-1-AP), ACTA2 (Sigma-Aldrich, #SAB5700835), KIM1 (Proteintech, #83221-2-RR), fibronectin (Abcam, #ab2413), DRP1 (Abcam, #ab184247), OXPHOS (Abcam, #ab110413), HA (Proteintech, #51064-2-AP), NMNAT1 (Sigma-Aldrich, #HPA059447), NMNAT2 (Sigma-Aldrich, #HPA015708), NMNAT3 (Sigma-Aldrich, #HPA039077), ACTIN (Proteintech, #HRP-60008), GAPDH (Proteintech, #HRP-60004), and TUBULIN (Proteintech, #66031-1-Ig). HRP-labeled goat anti-rabbit immunoglobulin G (IgG) (H + L) (Beyotime, #A0208) and HRP-labeled goat anti-mouse IgG (H + L) (Beyotime, #A0216) were used as a secondary antibody. Anti-rabbit IgG (H + L) (DyLight 800 4× PEG conjugate) (Cell Signaling Technology, #5151) and anti-mouse IgG (H + L) (DyLight 680 conjugate) (Cell Signaling Technology, #5470) were also used.

Fluorescent in situ hybridization

The paraffin-embedded section was subjected to dewaxing and dehydration, followed by boiling in the retrieval solution and subsequent natural cooling. Proteinase K (20 μg/ml) was added and incubated at 37°C for 15 min. Subsequently, it was washed with water and PBS. Each section was treated with prehybridization solution for 1 hour at 37°C. After removing the prehybridization solution, hybridization solution containing the probe was added, and overnight hybridization took place at 37°C in an incubator. The hybrid solution was washed off, followed by washing with 2× SSC. Last, the sections were incubated with primary antibodies, and then secondary antibodies were applied before imaging using a microscope.

mtDNA analysis

The determination of mtDNA copy number involves the calculation of the mtDNA/nDNA ratio, which is obtained by measuring mtDNA and nuclear DNA levels. Total DNA was extracted from kidney tissue using the TIANamp Genomic DNA Kit (TIANGEN, #4992254). The mtDNA/nDNA ratio was assessed through qPCR analysis targeting two mitochondrial genes [16*S* ribosomal RNA (rRNA) and ND1] and one nuclear gene (HK2 rRNA) (*83*), with primer sequences provided in table S2.

Live-cell imaging

Primary cultured renal PT cells were incubated with 100 nM MitoTracker (Beyotime, #C1035) for 30 min, followed by washing with PBS and direct imaging using a confocal microscope. For NAD^+ sensor imaging, cells were infected with FiNad- or SoNar-overexpressing lentivirus for a period of 48 hours, after which they were washed and directly imaged using a confocal microscope.

Mitochondrial membrane potential and mitochondrial superoxide assays

HEK293T cells, HK2 cells, or primary cultured renal PT cells were incubated in a 96-well plate and grown overnight reaching 70 to 80% confluency. Subsequently, the cells were exposed to 5 μM mitoSOX (Thermo Fisher Scientific, #M36008) for 10 min and analyzed using a plate reader with excitation/emission wavelengths set at 396/610 nm. In addition, the cells were incubated with JC-1 reagents from the mitochondrial membrane potential assay kit with JC-1 (Beyotime, #C2006) for a period of 20 min and measured using a plate reader at an excitation/emission of 490/530 nm.

Immunofluorescence staining

The cells were washed with PBS, fixed with 4% paraformaldehyde, permeabilized using PBS containing 0.2% Triton X-100, and subsequently blocked with 5% FBS. Immunostaining was carried out using the following primary antibodies: PPDPF (Proteintech, #19912-1-AP), KIM1 (R&D, #AF1817-SP), ATP5A1 (Proteintech, #66037-1-Ig), HSP60 (Proteintech, #66041-1-Ig), TOMM20 (Proteintech, #66777-1-Ig), NMNAT1 (Abcam, #ab118270; Sigma-Aldrich, #HPA059447), NMNAT2 (Abcam, #ab56980; Sigma-Aldrich, #HPA015708), NMNAT3 (Abcam, #ab71904; Sigma-Aldrich, #HPA039077), NAMPT (Thermo Fisher Scientific, #PA1-1045), vimentin (Proteintech, #10366-1-AP), fibronectin (Proteintech, #15613-1-AP), Col3a1 (Proteintech, #22734-1-AP), and LTL (Vector, #FL-1321-2).

Real-time qPCR

The RNA was extracted from mouse kidneys or cells using TRIzol reagent (Invitrogen) and reverse-transcribed into cDNA using HiScript III RT SuperMix (Vazyme, #R323). Real-time qPCR analysis was conducted using ChamQ Universal SYBR qPCR Master

Mix (Vazyme, #Q711). The primer pair sequences are provided in table S2.

Histopathology analysis

The kidneys were harvested from mice, rinsed in PBS, and fixed in 10% formalin and then subsequently in paraffin. Paraffin-embedded sections were subjected to H&E staining for histological analysis. Masson's trichrome and Picrosirius red staining were used to evaluate the extent of fibrosis. The degree of tubular injury was evaluated according to previously established scoring criteria (*81*).

NAD^+ measurement in extracts

For cell samples, the culture medium was aspirated and replaced with ice-cold NAD^+/NADH extraction buffer. Cells were gently resuspended by pipetting to facilitate lysis on ice or at room temperature. For tissue samples, specimens were dissected into small fragments and homogenized in NAD^+/NADH extraction buffer using a mechanical homogenizer. The resulting lysates were centrifuged at 12,000*g* for 10 min at 4°C, and the supernatant was collected for subsequent analysis. NAD^+ levels were quantified using the NAD^+/NADH Assay Kit with WST-8 (Beyotime, #S0175) according to the manufacturer's protocol.

Mitochondrial isolation

Cells were washed with PBS, treated with trypsin-EDTA solution, and subsequently centrifuged at 100 to 200*g* for 5 to 10 min at room temperature. The cells were gently resuspended in ice-cold PBS. A small aliquot of the cell suspension was taken for counting, while the remaining cells were centrifuged at 600*g* for 5 min at 4°C. After discarding the supernatant, 2 ml of mitochondria isolation reagent from the Cell Mitochondria Isolation Kit (Beyotime, #C3601) was added per 2×10^7 cells. The cells were gently resuspended and incubated on ice for 15 min. The cell suspension was then transferred to a glass homogenizer and homogenized 45 times. The resulting homogenate was centrifuged at 600*g* for 10 min at 4°C. The supernatant was carefully transferred to a new centrifuge tube and subjected to another centrifugation at 11,000*g* for 10 min at 4°C. The mitochondria were obtained from the resulting pellet after carefully removing the supernatant.

Complex I and NMNAT1 activity assay

Kidneys were harvested from mice, rinsed, and homogenized. The supernatant was subjected to NMNAT1 activity assay (Abcam, #ab221820) and complex I enzyme activity assay (Abcam, #ab109721), following the manufacturer's instructions.

Protein purification

PPDPF WT, C30S, C35S, and NMNAT1/2/3 proteins were purified as previously described (*84*). Briefly, proteins were expressed in Transetta (DE3) (Transgen Biotech), induced at optical density at 0.8 with 0.2 mM isopropyl-β-D-thiogalactopyranoside followed by at least 16 hours of expression at 18°C. The protein was bound to $Ni2^+$ ions-nitrilotriacetic acid Agarose (QIAGEN) and extensively washed with a solution containing 20 mM tris (pH 8.0), 500 mM NaCl, and 10% glycerol. Then, linear gradient elution was performed using a solution containing 500 mM imidazole, 20 mM tris (pH 8.0), 250 mM NaCl, and 10% glycerol. Fractions with more than 90% purity were dialyzed against a solution containing 150 mM KCl, 20 mM tris (pH 7.5), 1 mM dithiothreitol (DTT), and 10% glycerol. Then, the purified proteins were aliquoted and stored at −80°C.

Insulin turbidity assay

A total of 3 μM PPDPF WT, PPDPF C30S, or PPDPF C35S was respectively mixed with 100 μM insulin. Then, 1 μl of DTT was added before measuring theoptical density at 650 nm for 90 min. The reduction of insulin by DTT alone was used as a background.

Di-eosin glutathione disulfide assay

A total of 300 nM PPDPF WT, PPDPF C30S, or PPDPF C35S was respectively mixed with 150 nM di-eosin-GSSG. Just before starting the measurement, DTT was added to achieve a final concentration of 5 μM. The total reaction volume was 200 μl. The reaction mix was transferred to a well in a 96-well black plate, and fluorescence was measured at excitation/emission wavelengths of 520/550 nm for 30 min. Background fluorescence was determined by measuring the reduction of 150 nM di-eosin-GSSG by 5 μM DTT alone.

Denatured RNase disulfide isomerase assay

The reaction mixture was prepared using 8 mM denatured RNase, 1 mM glutathione, 0.2 mM GSSG, and 4.5 mM cyclic pyrimidine nucleotides cytidine 3′,5′-cyclic monophosphate (cCMP) in a pH 8.0 buffer composed of 55 mM tris/acetate and 1 mM EDTA. PPDPF WT, PPDPF C30S, or PPDPF C35S protein was added to the mixture at a concentration of 3 μM. Denatured reduced RNase was replaced with native RNase by adding 2.5 μl of the latter to achieve a final concentration of 40 μM. The hydrolysis of cCMP by native RNase at a concentration of 40 μM was designated as representing full enzymatic activity (100%). The background signal was determined by measuring the hydrolysis of cCMP by denatured reduced RNase alone. The absorbance of the solution at 296 nm was monitored continuously for 30 min to quantify RNase activity.

Redox potential determination

Fifteen reactions were prepared in 0.6-ml tubes, each containing 45 μl of "substrate stock 1" (1.1 μM substrate protein and 0.55 mM DTTox in PBS with 0.1 mM EDTA). Separate stocks of DTTred were prepared at a 10× final concentration by first creating a 100 mM stock of DTTred in PBS and 0.1 mM EDTA. This stock was added to the tubes containing substrate stock 1 to establish varying ratios of DTTred/DTTox, which define the redox-buffering environment for the disulfide bond. After adding 5 μl of each prepared DTTred stock to the corresponding substrate stock 1, the reactions were mixed thoroughly. To minimize oxidation during incubation, the microcentrifuge tubes were quickly flushed with argon gas before sealing. The sealed tubes were incubated at 25°C for an 18 hours until redox equilibrium was reached. The temperature may vary depending on the calculation of the standard redox potential. To label free thiols in the reaction, 5 μl of a 55 mM MPB stock was added to each reaction, yielding a final concentration of 5 mM MPB. The reactions were incubated with MPB for 1 hour at the defined temperature to ensure complete thiol labeling. Excess unreacted MPB was quenched by adding 5 mM glutathione and incubating at room temperature for 60 min. Nonreducing protein loading buffer was added to the samples, and the redox state of the proteins was analyzed using an SDS-gel shift assay on a 4 to 20% polyacrylamide gradient gel.

Proximity ligation assay

After incubation with primary antibodies, PLA was performed using 20 μl of reaction per step per slide according to the Sigma-Aldrich Duolink In Situ PLA manufacturer's instructions (Sigma-Aldrich, catalog no. DUO92101). Briefly, two PLA secondary probes, anti-mouse MINUS (targeting anti-NMNAT1/2/3 mouse primary) and anti-rabbit PLUS (targeting anti-PPDPF rabbit primary), were diluted 1:5 in antibody diluent buffer provided by the manufacturer and incubated 1 hour at 37°C. Slides were washed in twice wash buffer A for 10 min. For the following ligation reaction, PLA ligation stock was diluted 1:5 in distilled H_2O with ligase (added at 1:40), and then slides were incubated for 30 min at 37°C. Slides were then washed twice in wash buffer A for 10 min, and then the PLA amplification reaction buffer was added (1:5 amplification stock and 1:80 polymerase diluted in distilled H_2O), and slides were incubated for 100 min at 37°C. Slides were then washed twice with 1× wash buffer B for 10 min and 0.01 wash buffer B for 1 min. After mounted with mounting Mmdium (with 4′,6-diamidino-2-phenylindole), images were taken using confocal microscope with a 100× oil immersion objectives.

Statistical analysis

The statistical analyses were conducted using GraphPad Prism software (GraphPad Software Inc., La Jolla, CA). A two-tailed *t* test was used for comparing two groups, while one-way or two-way analysis of variance (ANOVA) was used for comparing multiple groups. All data are presented as mean ± SEM. Statistical significance was defined as *P* values less than 0.05.

Supplementary Materials

This PDF file includes:
Figs. S1 to S15
Tables S1 and S2

REFERENCES AND NOTES

1. J. Bragg-Gresham, X. Zhang, D. Le, M. Heung, V. Shahinian, H. Morgenstern, R. Saran, Prevalence of chronic kidney disease among Black individuals in the US after removal of the Black race coefficient from a glomerular filtration rate estimating equation. *JAMA Netw. Open.* **4**, e2035636 (2021).
2. C. P. Kovesdy, Epidemiology of chronic kidney disease: An update 2022. *Kidney Int. Suppl.* **12**, 7–11 (2022).
3. A. Kottgen, N. L. Glazer, A. Dehghan, S. J. Hwang, R. Katz, M. Li, Q. Yang, V. Gudnason, L. J. Launer, T. B. Harris, A. V. Smith, D. E. Arking, B. C. Astor, E. Boerwinkle, G. B. Ehret, I. Ruczinski, R. B. Scharpf, Y. D. Chen, I. H. de Boer, T. Haritunians, T. Lumley, M. Sarnak, D. Siscovick, E. J. Benjamin, D. Levy, A. Upadhyay, Y. S. Aulchenko, A. Hofman, F. Rivadeneira, A. G. Uitterlinden, C. M. van Duijn, D. I. Chasman, G. Pare, P. M. Ridker, W. H. Kao, J. C. Witteman, J. Coresh, M. G. Shlipak, C. S. Fox, Multiple loci associated with indices of renal function and chronic kidney disease. *Nat. Genet.* **41**, 712–717 (2009).
4. C. Pattaro, A. Teumer, M. Gorski, A. Y. Chu, M. Li, V. Mijatovic, M. Garnaas, A. Tin, R. Sorice, Y. Li, D. Taliun, M. Olden, M. Foster, Q. Yang, M. H. Chen, T. H. Pers, A. D. Johnson, Y. A. Ko, C. Fuchsberger, B. Tayo, M. Nalls, M. F. Feitosa, A. Isaacs, A. Dehghan, P. d'Adamo, A. Adeyemo, A. K. Dieffenbach, A. B. Zonderman, I. M. Nolte, P. J. van der Most, A. F. Wright, A. R. Shuldiner, A. C. Morrison, A. Hofman, A. V. Smith, A. W. Dreisbach, A. Franke, A. G. Uitterlinden, A. Metspalu, A. Tonjes, A. Lupo, A. Robino, A. Johansson, A. Demirkan, B. Kollerits, B. I. Freedman, B. Ponte, B. A. Oostra, B. Paulweber, B. K. Kramer, B. D. Mitchell, B. M. Buckley, C. A. Peralta, C. Hayward, C. Helmer, C. N. Rotimi, C. M. Shaffer, C. Muller, C. Sala, C. M. van Duijn, A. Saint-Pierre, D. Ackermann, D. Shriner, D. Ruggiero, D. Toniolo, Y. Lu, D. Cusi, D. Czamara, D. Ellinghaus, D. S. Siscovick, D. Ruderfer, C. Gieger, H. Grallert, E. Rochtchina, E. J. Atkinson, E. G. Holliday, E. Boerwinkle, E. Salvi, E. P. Bottinger, F. Murgia, F. Rivadeneira, F. Ernst, F. Kronenberg, F. B. Hu, G. J. Navis, G. C. Curhan, G. B. Ehret, G. Homuth, S. Coassin, G. A. Thun, G. Pistis, G. Gambaro, G. Malerba, G. W. Montgomery, G. Eiriksdottir, G. Jacobs, G. Li, H. E. Wichmann, H. Campbell, H. Schmidt, H. Wallaschofski, H. Volzke, H. Brenner, H. K. Kroemer, H. Kramer, H. Lin, I. M. Leach, I. Ford, I. Guessous, I. Rudan, I. Prokopenko, I. Borecki, I. M. Heid, I. Kolcic, I. Persico, J. W. Jukema, J. F. Wilson, J. F. Felix, J. Divers, J. C. Lambert, J. M. Stafford, J. M. Gaspoz, J. A. Smith, J. D. Faul, J. J. Wang, J. Ding, J. N. Hirschhorn, J. Attia, J. B. Whitfield, J. Chalmers, J. Viikari, J. Coresh, J. C. Denny, J. Karjalainen, J. K. Fernandes, K. Endlich, K. Butterbach, K. L. Keene, K. Lohman, L. Portas, L. J. Launer, L. P. Lyytikainen, L. Yengo, L. Franke, L. Ferrucci, L. M. Rose, L. Kedenko, M. Rao, M. Struchalin, M. E. Kleber, M. Cavalieri, M. Haun, M. C. Cornelis, M. Ciullo, M. Pirastu, M. de Andrade, M. A. McEvoy, M. Woodward, M. Adam, M. Cocca, M. Nauck, M. Imboden, M. Waldenberger, M. Pruijm, M. Metzger, M. Stumvoll, M. K. Evans, M. M. Sale, M. Kahonen, M. Boban, M. Bochud, M. Rheinberger, N. Verweij, N. Bouatia-Naji, N. G. Martin, N. Hastie, N. Probst-Hensch, N. Soranzo, O. Devuyst, O. Raitakari, O. Gottesman, O. H. Franco, O. Polasek, P. Gasparini, P. B. Munroe, P. M. Ridker, P. Mitchell, P. Muntner, C. Meisinger, J. H. Smit, I. Consortium, A. Consortium, C. H.-H. F. G. Cardiogram, E. C. Consortium, P. Kovacs, P. S. Wild, P. Froguel, R. Rettig, R. Magi, R. Biffar, R. Schmidt, R. P. Middelberg, R. J. Carroll, B. W. Penninx, R. J. Scott, R. Katz, S. Sedaghat, S. H. Wild, S. L. Kardia, S. Ulivi, S. J. Hwang, S. Enroth, S. Kloiber, S. Trompet, B. Stengel, S. J. Hancock, S. T. Turner, S. E. Rosas, S. Stracke, T. B. Harris, T. Zeller, T. Zemunik, T. Lehtimaki, T. Illig, T. Aspelund, T. Nikopensius, T. Esko, T. Tanaka, U. Gyllensten, U. Volker, V. Emilsson, V. Vitart, V. Aalto, V. Gudnason, V. Chouraki, W. M. Chen, W. Igl, W. Marz, W. Koenig, W. Lieb, R. J. Loos, Y. Liu, H. Snieder, P. P. Pramstaller, A. Parsa, J. R. O'Connell, K. Susztak, P. Hamet, J. Tremblay, I. H. de Boer, C. A. Boger, W. Goessling, D. I. Chasman, A. Kottgen, W. H. Kao, C. S. Fox, Genetic associations at 53 loci highlight cell types and biological pathways relevant for kidney function. *Nat. Commun.* **7**, 10023 (2016).
5. M. Wuttke, Y. Li, M. Li, K. B. Sieber, M. F. Feitosa, M. Gorski, A. Tin, L. Wang, A. Y. Chu, A. Hoppmann, H. Kirsten, A. Giri, J. F. Chai, G. Sveinbjornsson, B. O. Tayo, T. Nutile, C. Fuchsberger, J. Marten, M. Cocca, S. Ghasemi, Y. Xu, K. Horn, D. Noce, P. J. van der Most, S. Sedaghat, Z. Yu, M. Akiyama, S. Afaq, T. S. Ahluwalia, P. Almgren, N. Amin, J. Arnlov, S. J. L. Bakker, N. Bansal, D. Baptista, S. Bergmann, M. L. Biggs, G. Biino, M. Boehnke, E. Boerwinkle, M. Boissel, E. P. Bottinger, T. S. Boutin, H. Brenner, M. Brumat, R. Burkhardt, A. S. Butterworth, E. Campana, A. Campbell, H. Campbell, M. Canouil, R. J. Carroll, E. Catamo, J. C. Chambers, M. L. Chee, M. L. Chee, X. Chen, C. Y. Cheng, Y. Cheng, K. Christensen, R. Cifkova, M. Ciullo, M. P. Concas, J. P. Cook, J. Coresh, T. Corre, C. F. Sala, D. Cusi, J. Danesh, E. W. Daw, M. H. de Borst, A. De Grandi, R. de Mutsert, A. P. J. de Vries, F. Degenhardt, G. Delgado, A. Demirkan, E. Di Angelantonio, K. Dittrich, J. Divers, R. Dorajoo, K. U. Eckardt, G. Ehret, P. Elliott, K. Endlich, M. K. Evans, J. F. Felix, V. H. X. Foo, O. H. Franco, A. Franke, B. I. Freedman, S. Freitag-Wolf, Y. Friedlander, P. Froguel, R. T. Gansevoort, H. Gao, P. Gasparini, J. M. Gaziano, V. Giedraitis, C. Gieger, G. Girotto, F. Giulianini, M. Gogele, S. D. Gordon, D. F. Gudbjartsson, V. Gudnason, T. Haller, P. Hamet, T. B. Harris, C. A. Hartman, C. Hayward, J. N. Hellwege, C. K. Heng, A. A. Hicks, E. Hofer, W. Huang, N. Hutri-Kahonen, S. J. Hwang, M. A. Ikram, O. S. Indridason, E. Ingelsson, M. Ising, V. W. V. Jaddoe, J. Jakobsdottir, J. B. Jonas, P. K. Joshi, N. S. Josyula, B. Jung, M. Kahonen, Y. Kamatani, C. M. Kammerer, M. Kanai, M. Kastarinen, S. M. Kerr, C. C. Khor, W. Kiess, M. E. Kleber, W. Koenig, J. S. Kooner, A. Korner, P. Kovacs, A. T. Kraja, A. Krajcoviechova, H. Kramer, B. K. Kramer, F. Kronenberg, M. Kubo, B. Kuhnel, M. Kuokkanen, J. Kuusisto, M. La Bianca, M. Laakso, L. A. Lange, C. D. Langefeld, J. J. Lee, B. Lehne, T. Lehtimaki, W. Lieb, S. L. Cohort, S. C. Lim, L. Lind, C. M. Lindgren, J. Liu, J. Liu, M. Loeffler, R. J. F. Loos, S. Lucae, M. A. Lukas, L. P. Lyytikainen, R. Magi, P. K. E. Magnusson, A. Mahajan, N. G. Martin, J. Martins, W. Marz, D. Mascalzoni, K. Matsuda, C. Meisinger, T. Meitinger, O. Melander, A. Metspalu, E. K. Mikaelsdottir, Y. Milaneschi, K. Miliku, P. P. Mishra, V. A. M. V. Program, K. L. Mohlke, N. Mononen, G. W. Montgomery, D. O. Mook-Kanamori, J. C. Mychaleckyj, G. N. Nadkarni, M. A. Nalls, M. Nauck, K. Nikus, B. Ning, I. M. Nolte, R. Noordam, J. O'Connell, M. L. O'Donoghue, I. Olafsson, A. J. Oldehinkel, M. Orho-Melander, W. H. Ouwehand, S. Padmanabhan, N. D. Palmer, R. Palsson, B. Penninx, T. Perls, M. Perola, M. Pirastu, N. Pirastu, G. Pistis, A. I. Podgornaia, O. Polasek, B. Ponte, D. J. Porteous, T. Poulain, P. P. Pramstaller, M. H. Preuss, B. P. Prins, M. A. Province, T. J. Rabelink, L. M. Raffield, O. T. Raitakari, D. F. Reilly, R. Rettig, M. Rheinberger, K. M. Rice, P. M. Ridker, F. Rivadeneira, F. Rizzi, D. J. Roberts, A. Robino, P. Rossing, I. Rudan, R. Rueedi, D. Ruggiero, K. A. Ryan, Y. Saba, C. Sabanayagam, V. Salomaa, E. Salvi, K. U. Saum, H. Schmidt, R. Schmidt, B. Schottker, C. A. Schulz, N. Schupf, C. M. Shaffer, Y. Shi, A. V. Smith, B. H. Smith, N. Soranzo, C. N. Spracklen, K. Strauch, H. M. Stringham, M. Stumvoll, P. O. Svensson, S. Szymczak, E. S. Tai, S. M. Tajuddin, N. Y. Q. Tan, K. D. Taylor, A. Teren, Y. C. Tham, J. Thiery, C. H. L. Thio, H. Thomsen, G. Thorleifsson, D. Toniolo, A. Tonjes, J. Tremblay, I. Tzoulaki, A. G. Uitterlinden, S. Vaccargiu, R. M. van Dam, P. van der Harst, C. M. van Duijn, D. R. V. Edward, N. Verweij, S. Vogelezang, U. Volker, P. Vollenweider, G. Waeber, M. Waldenberger, L. Wallentin, Y. X. Wang, C. Wang, D. M. Waterworth, W. B. Wei, H. White, J. B. Whitfield, S. H. Wild, J. F. Wilson, M. K. Wojczynski, C. Wong, T. Y. Wong, L. Xu, Q. Yang, M. Yasuda, L. M. Yerges-Armstrong, W. Zhang, A. B. Zonderman, J. I. Rotter, M. Bochud, B. M. Psaty, V. Vitart, J. G. Wilson, A. Dehghan, A. Parsa, D. I. Chasman, K. Ho, A. P. Morris, O. Devuyst, S. Akilesh, S. A. Pendergrass, X. Sim, C. A. Boger, Y. Okada, T. L. Edwards, H. Snieder, K. Stefansson, A. M. Hung, I. M. Heid, M. Scholz, A. Teumer, A. Kottgen, C. Pattaro, A catalog of genetic loci associated with kidney function from analyses of a million individuals. *Nat. Genet.* **51**, 957–972 (2019).
6. J. N. Hellwege, D. R. V. Edwards, A. Giri, C. Qiu, J. Park, E. S. Torstenson, J. M. Keaton, O. D. Wilson, C. Robinson-Cohen, C. P. Chung, C. L. Roumie, D. Klarin, S. M. Damrauer, S. L. Du Vall, E. Siew, E. A. Akwo, M. Wuttke, M. Gorski, M. Li, Y. Li, J. M. Gaziano, P. W. F. Wilson, P. S. Tsao, C. J. O'Donnell, C. P. Kovesdy, C. Pattaro, A. Köttgen, K. Susztak, T. L. Edwards, A. M. Hung, Mapping eGFR loci to the renal transcriptome and phenome in the VA Million Veteran Program. *Nat. Commun.* **10**, 3842 (2019).

7. H. Liu, T. Doke, D. Guo, X. Sheng, Z. Ma, J. Park, H. M. T. Vy, G. N. Nadkarni, A. Abedini, Z. Miao, M. Palmer, B. F. Voight, H. Li, C. D. Brown, M. D. Ritchie, Y. Shu, K. Susztak, Epigenomic and transcriptomic analyses define core cell types, genes and targetable mechanisms for kidney disease. *Nat. Genet.* **54**, 950–962 (2022).
8. S. L. Edwards, J. Beesley, J. D. French, A. M. Dunning, Beyond GWASs: Illuminating the dark road from association to function. *Am. J. Hum. Genet.* **93**, 779–797 (2013).
9. P. Dhillon, J. Park, C. Hurtado Del Pozo, L. Li, T. Doke, S. Huang, J. Zhao, H. M. Kang, R. Shrestra, M. S. Balzer, S. Chatterjee, P. Prado, S. Y. Han, H. Liu, X. Sheng, P. Dierickx, K. Batmanov, J. P. Romero, F. Prosper, M. Li, L. Pei, J. Kim, N. Montserrat, K. Susztak, The nuclear receptor ESRRA protects from kidney disease by coupling metabolism and differentiation. *Cell Metab.* **33**, 379–394.e8 (2021).
10. T. Doke, A. Abedini, D. L. Aldridge, Y. W. Yang, J. Park, C. M. Hernandez, M. S. Balzer, R. Shrestra, G. Coppock, J. M. I. Rico, S. Y. Han, J. Kim, S. Xin, A. M. Piliponsky, M. Angelozzi, V. Lefebvre, M. C. Siracusa, C. A. Hunter, K. Susztak, Single-cell analysis identifies the interaction of altered renal tubules with basophils orchestrating kidney fibrosis. *Nat. Immunol.* **23**, 947–959 (2022).
11. F. Schreibing, R. Kramann, Mapping the human kidney using single-cell genomics. *Nat. Rev. Nephrol.* **18**, 347–360 (2022).
12. A. M. Hall, S. de Seigneux, Metabolic mechanisms of acute proximal tubular injury. *Pflugers Arch.* **474**, 813–827 (2022).
13. M. Chang-Panesso, B. D. Humphreys, Cellular plasticity in kidney injury and repair. *Nat. Rev. Nephrol.* **13**, 39–46 (2017).
14. D. E. Discher, P. Janmey, Y. L. Wang, Tissue cells feel and respond to the stiffness of their substrate. *Science* **310**, 1139–1143 (2005).
15. J. Irianto, C. R. Pfeifer, Y. Xia, D. E. Discher, SnapShot: Mechanosensing matrix. *Cell* **165**, 1820–e1821 (2016).
16. N. Nowak, J. Skupien, M. A. Niewczas, M. Yamanouchi, M. Major, S. Croall, A. Smiles, J. H. Warram, J. V. Bonventre, A. S. Krolewski, Increased plasma kidney injury molecule-1 suggests early progressive renal decline in non-proteinuric patients with type 1 diabetes. *Kidney Int.* **89**, 459–467 (2016).
17. Q.-W. Zheng, Q.-Z. Ni, B. Zhu, X. Liang, N. Ma, Y.-K. Wang, S. Xu, H.-J. Cao, J. Xia, F.-K. Zhang, E.-B. Zhang, X.-S. Qiu, X.-F. Ding, L. Qiu, X.-L. Zhang, Z.-H. Dong, Z.-G. Li, X.-L. Zhang, D. Xie, J.-J. Li, PPDPF promotes lung adenocarcinoma progression via inhibiting apoptosis and NK cell-mediated cytotoxicity through STAT3. *Oncogene* **41**, 4244–4256 (2022).
18. Q.-Z. Ni, B. Zhu, Y. Ji, Q.-W. Zheng, X. Liang, N. Ma, H. Jiang, F.-K. Zhang, Y.-R. Shang, Y.-K. Wang, S. Xu, E.-B. Zhang, Y.-M. Yuan, T.-W. Chen, F.-F. Yin, H.-J. Cao, J.-Y. Huang, J. Xia, X.-F. Ding, X.-S. Qiu, K. Ding, C. Song, W.-T. Zhou, M. Wu, K. Wang, R. Lui, Q. Lin, W. Chen, Z.-G. Li, S.-Q. Cheng, X.-F. Wang, D. Xie, J.-J. Li, PPDPF promotes the development of mutant KRAS-driven pancreatic ductal adenocarcinoma by regulating the GEF activity of SOS1. *Adv. Sci.* **10**, e2202448 (2023).
19. Z. Miao, M. S. Balzer, Z. Ma, H. Liu, J. Wu, R. Shrestha, T. Aranyi, A. Kwan, A. Kondo, M. Pontoglio, J. Kim, M. Li, K. H. Kaestner, K. Susztak, Single cell regulatory landscape of the mouse kidney highlights cellular differentiation programs and disease targets. *Nat. Commun.* **12**, 2277 (2021).
20. K. J. Stanzick, Y. Li, P. Schlosser, M. Gorski, M. Wuttke, L. F. Thomas, H. Rasheed, B. X. Rowan, S. E. Graham, B. R. Vanderweff, S. B. Patil, VA Million Veteran Program, C. Robinson-Cohen, J. M. Gaziano, C. J. O'Donnell, C. J. Willer, S. Hallan, B. O. Åsvold, A. Gessner, A. M. Hung, C. Pattaro, A. Köttgen, K. J. Stark, I. M. Heid, T. W. Winkler, Discovery and prioritization of variants and genes for kidney function in >1.2 million individuals. *Nat. Commun.* **12**, 4350 (2021).
21. C. Qiu, S. Huang, J. Park, Y. Park, Y. A. Ko, M. J. Seasock, J. S. Bryer, X. X. Xu, W. C. Song, M. Palmer, J. Hill, P. Guarnieri, J. Hawkins, C. M. Boustany-Kari, S. S. Pullen, C. D. Brown, K. Susztak, Renal compartment-specific genetic variation analyses identify new pathways in chronic kidney disease. *Nat. Med.* **24**, 1721–1731 (2018).
22. X. Sheng, Y. Guan, Z. Ma, J. Wu, H. Liu, C. Qiu, S. Vitale, Z. Miao, M. J. Seasock, M. Palmer, M. K. Shin, K. L. Duffin, S. S. Pullen, T. L. Edwards, J. N. Hellwege, A. M. Hung, M. Li, B. F. Voight, T. M. Coffman, C. D. Brown, K. Susztak, Mapping the genetic architecture of human traits to cell types in the kidney identifies mechanisms of disease and potential treatments. *Nat. Genet.* **53**, 1322–1333 (2021).
23. A. Lu, M. A. Pallero, B. Y. Owusu, A. V. Borovjagin, W. Lei, P. W. Sanders, J. E. Murphy-Ullrich, Calreticulin is important for the development of renal fibrosis and dysfunction in diabetic nephropathy. *Matrix Biol. Plus.* **8**, 100034 (2020).
24. C. Zheng, L. Huang, W. Luo, W. Yu, X. Hu, X. Guan, Y. Cai, C. Zou, H. Yin, Z. Xu, G. Liang, Y. Wang, Inhibition of STAT3 in tubular epithelial cells prevents kidney fibrosis and nephropathy in STZ-induced diabetic mice. *Cell Death Dis.* **10**, 848 (2019).
25. S. K. Han, M. T. McNulty, C. J. Benway, P. Wen, A. Greenberg, A. C. Onuchic-Whitford, Nephrotic Syndrome Study, D. Jang, J. Flannick, N. P. Burtt, P. C. Wilson, B. D. Humphreys, X. Wen, Z. Han, D. Lee, M. G. Sampson, Mapping genomic regulation of kidney disease and traits through high-resolution and interpretable eQTLs. *Nat. Commun.* **14**, 2229 (2023).
26. H. Li, E. E. Dixon, H. Wu, B. D. Humphreys, Comprehensive single-cell transcriptional profiling defines shared and unique epithelial injury responses during kidney fibrosis. *Cell Metab.* **34**, 1977–1998.e9 (2022).
27. M. Park, C. H. Kwon, H. K. Ha, M. Han, S. H. Song, RNA-seq identifies condition-specific biological signatures of ischemia-reperfusion injury in the human kidney. *BMC Nephrol.* **21**, 398 (2020).
28. M. S. Balzer, T. Doke, Y. W. Yang, D. L. Aldridge, H. Hu, H. Mai, D. Mukhi, Z. Ma, R. Shrestha, M. B. Palmer, C. A. Hunter, K. Susztak, Single-cell analysis highlights differences in druggable pathways underlying adaptive or fibrotic kidney regeneration. *Nat. Commun.* **13**, 4018 (2022).
29. C. M. McEvoy, J. M. Murphy, L. Zhang, S. Clotet-Freixas, J. A. Mathews, J. An, M. Karimzadeh, D. Pouyabahar, S. Su, O. Zaslaver, H. Röst, R. Arambewela, L. Y. Liu, S. Zhang, K. A. Lawson, A. Finelli, B. Wang, S. A. MacParland, G. D. Bader, A. Konvalinka, S. Q. Crome, Single-cell profiling of healthy human kidney reveals features of sex-based transcriptional programs and tissue-specific immunity. *Nat. Commun.* **13**, 7634 (2022).
30. P. C. Wilson, H. Wu, Y. Kirita, K. Uchimura, N. Ledru, H. G. Rennke, P. A. Welling, S. S. Waikar, B. D. Humphreys, The single-cell transcriptomic landscape of early human diabetic nephropathy. *Proc. Natl. Acad. Sci. U.S.A.* **116**, 19619–19625 (2019).
31. B. B. Lake, R. Menon, S. Winfree, Q. Hu, R. M. Ferreira, K. Kalhor, D. Barwinska, E. A. Otto, M. Ferkowicz, D. Diep, N. Plongthongkum, A. Knoten, S. Urata, L. H. Mariani, A. S. Naik, S. Eddy, B. Zhang, Y. Wu, D. Salamon, J. C. Williams, X. Wang, K. S. Balderrama, P. J. Hoover, E. Murray, J. L. Marshall, T. Noel, A. Vijayan, A. Hartman, F. Chen, S. S. Waikar, S. E. Rosas, F. P. Wilson, P. M. Palevsky, K. Kiryluk, J. R. Sedor, R. D. Toto, C. R. Parikh, E. H. Kim, R. Satija, A. Greka, E. Z. Macosko, P. V. Kharchenko, J. P. Gaut, J. B. Hodgin, KPMP Consortium, M. T. Eadon, P. C. Dagher, T. M. El-Achkar, K. Zhang, M. Kretzler, S. Jain, An atlas of healthy and injured cell states and niches in the human kidney. *Nature* **619**, 585–594 (2023).
32. L. Machado, P. Geara, J. Camps, M. D. Santos, F. Teixeira-Clerc, J. Van Herck, H. Varet, R. Legendre, J.-M. Pawlotsky, M. Sampaolesi, T. Voet, P. Maire, F. Relaix, P. Mourikis, Tissue damage induces a conserved stress response that initiates quiescent muscle stem cell activation. *Cell Stem Cell* **28**, 1125–1135.e7 (2021).
33. Y. Shao, Y. Guan, L. Wang, Z. Qiu, M. Liu, Y. Chen, L. Wu, Y. Li, X. Ma, M. Liu, D. Li, CRISPR/Cas-mediated genome editing in the rat via direct injection of one-cell embryos. *Nat. Protoc.* **9**, 2493–2512 (2014).
34. K. S. Peterson, J.-F. Huang, J. Zhu, V. D'Agati, X. Liu, N. Miller, M. G. Erlander, M. R. Jackson, R. J. Winchester, Characterization of heterogeneity in the molecular pathogenesis of lupus nephritis from transcriptional profiles of laser-captured glomeruli. *J. Clin. Invest.* **113**, 1722–1733 (2004).
35. Y. Zou, A. Wang, L. Huang, X. Zhu, Q. Hu, Y. Zhang, X. Chen, F. Li, Q. Wang, H. Wang, R. Liu, F. Zuo, T. Li, J. Yao, Y. Qian, M. Shi, X. Yue, W. Chen, Z. Zhang, C. Wang, Y. Zhou, L. Zhu, Z. Ju, J. Loscalzo, Y. Yang, Y. Zhao, Illuminating NAD$^+$ metabolism in live cells and in vivo using a genetically encoded fluorescent sensor. *Dev. Cell* **53**, 240–252.e7 (2020).
36. Y. Zhao, Q. Hu, F. Cheng, N. Su, A. Wang, Y. Zou, H. Hu, X. Chen, H. M. Zhou, X. Huang, K. Yang, Q. Zhu, X. Wang, J. Yi, L. Zhu, X. Qian, L. Chen, Y. Tang, J. Loscalzo, Y. Yang, SoNar, a highly responsive NAD$^+$/NADH sensor, allows high-throughput metabolic screening of anti-tumor agents. *Cell Metab.* **21**, 777–789 (2015).
37. F. E. El-Rami, A. E. Sikora, Bioinformatics workflow for gonococcal proteomics. *Methods Mol. Biol.* **1997**, 185–205 (2019).
38. C. S. Yu, Y. C. Chen, C. H. Lu, J. K. Hwang, Prediction of protein subcellular localization. *Proteins* **64**, 643–651 (2006).
39. J. M. Brazill, C. Li, Y. Zhu, R. G. Zhai, NMNAT: It's an NAD$^+$ synthase… It's a chaperone… It's a neuroprotector. *Curr. Opin. Genet. Dev.* **44**, 156–162 (2017).
40. K. Tunyasuvunakool, J. Adler, Z. Wu, T. Green, M. Zielinski, A. Žídek, A. Bridgland, A. Cowie, C. Meyer, A. Laydon, S. Velankar, G. J. Kleywegt, A. Bateman, R. Evans, A. Pritzel, M. Figurnov, O. Ronneberger, R. Bates, S. A. A. Kohl, A. Potapenko, A. J. Ballard, B. Romera-Paredes, S. Nikolov, R. Jain, E. Clancy, D. Reiman, S. Petersen, A. W. Senior, K. Kavukcuoglu, E. Birney, P. Kohli, J. Jumper, D. Hassabis, Highly accurate protein structure prediction for the human proteome. *Nature* **596**, 590–596 (2021).
41. A. M. Lesk, NAD-binding domains of dehydrogenases. *Curr. Opin. Struct. Biol.* **5**, 775–783 (1995).
42. L. A. Kelley, S. Mezulis, C. M. Yates, M. N. Wass, M. J. Sternberg, The Phyre2 web portal for protein modeling, prediction and analysis. *Nat. Protoc.* **10**, 845–858 (2015).
43. Q. A. Sun, L. Kirnarsky, S. Sherman, V. N. Gladyshev, Selenoprotein oxidoreductase with specificity for thioredoxin and glutathione systems. *Proc. Natl. Acad. Sci. U.S.A.* **98**, 3673–3678 (2001).
44. A. E. Pijning, P. Hogg, Classification of protein disulphide bonds. *Methods Mol. Biol.* **1967**, 1–8 (2019).
45. E. Pedone, B. Ren, R. Ladenstein, M. Rossi, S. Bartolucci, Functional properties of the protein disulfide oxidoreductase from the archaeon Pyrococcus furiosus: A member of a novel protein family related to protein disulfide-isomerase. *Eur. J. Biochem.* **271**, 3437–3448 (2004).
46. H. Peng, W. Chen, Y. Cheng, L. Hakuna, R. Strongin, B. Wang, Thiol reactive probes and chemosensors. *Sensors* **12**, 15907–15946 (2012).
47. T. Doke, K. Susztak, The multifaceted role of kidney tubule mitochondrial dysfunction in kidney disease development. *Trends Cell Biol.* **32**, 841–853 (2022).
48. K. M. Ralto, E. P. Rhee, S. M. Parikh, NAD$^+$ homeostasis in renal health and disease. *Nat. Rev. Nephrol.* **16**, 99–111 (2020).

49. N. Ma, Y.-K. Wang, S. Xu, Q.-Z. Ni, Q.-W. Zheng, B. Zhu, H.-J. Cao, H. Jiang, F.-K. Zhang, Y.-M. Yuan, E.-B. Zhang, T.-W. Chen, J. Xia, X.-F. Ding, Z.-H. Chen, X.-P. Zhang, K. Wang, S.-Q. Cheng, L. Qiu, Z.-G. Li, Y.-C. Yu, X.-F. Wang, B. Zhou, J.-J. Li, D. Xie, PPDPF alleviates hepatic steatosis through inhibition of mTOR signaling. *Nat. Commun.* **12**, 3059 (2021).
50. C. N. Sharp, M. A. Doll, T. V. Dupre, P. P. Shah, M. Subathra, D. Siow, G. E. Arteel, J. Megyesi, L. J. Beverly, L. J. Siskind, Repeated administration of low-dose cisplatin in mice induces fibrosis. *Am. J. Physiol. Renal Physiol.* **310**, F560–F568 (2016).
51. Y. Fu, J. Cai, F. Li, Z. Liu, S. Shu, Y. Wang, Y. Liu, C. Tang, Z. Dong, Chronic effects of repeated low-dose cisplatin treatment in mouse kidneys and renal tubular cells. *Am. J. Physiol. Renal Physiol.* **317**, F1582–F1592 (2019).
52. E. Galfetti, A. Cerutti, M. Ghielmini, E. Zucca, L. Wannesson, Risk factors for renal toxicity after inpatient cisplatin administration. *BMC Pharmacol. Toxicol.* **21**, 19 (2020).
53. Z. He, C. Song, S. Li, C. Dong, W. Liao, Y. Xiong, S. Yang, Y. Liu, Development and application of the CRISPR-dcas13d-eIF4G translational regulatory system to inhibit ferroptosis in calcium oxalate crystal-induced kidney injury. *Adv. Sci.* **11**, e2309234 (2024).
54. Q.-Q. Chen, K. Liu, N. Shi, G. Ma, P. Wang, H.-M. Xie, S.-J. Jin, T.-T. Wei, X.-Y. Yu, Y. Wang, J.-Y. Zhang, P. Li, L.-W. Qi, L. Zhang, Neuraminidase 1 promotes renal fibrosis development in male mice. *Nat. Commun.* **14**, 1713 (2023).
55. F. L. Craciun, V. Bijol, A. K. Ajay, P. Rao, R. K. Kumar, J. Hutchinson, O. Hofmann, N. Joshi, J. P. Luyendyk, U. Kusebauch, C. L. Moss, A. Srivastava, J. Himmelfarb, S. S. Waikar, R. L. Moritz, V. S. Vaidya, RNA sequencing identifies novel translational biomarkers of kidney fibrosis. *J. Am. Soc. Nephrol.* **27**, 1702–1713 (2016).
56. E. Arvaniti, P. Moulos, A. Vakrakou, C. Chatziantoniou, C. Chadjichristos, P. Kavvadas, A. Charonis, P. K. Politis, Whole-transcriptome analysis of UUO mouse model of renal fibrosis reveals new molecular players in kidney diseases. *Sci. Rep.* **6**, 26235 (2016).
57. P. Beckerman, C. Qiu, J. Park, N. Ledo, Y. A. Ko, A. D. Park, S. Y. Han, P. Choi, M. Palmer, K. Susztak, Human kidney tubule-specific gene expression based dissection of chronic kidney disease traits. *EBioMedicine* **24**, 267–276 (2017).
58. M. I. Choudhury, Y. Li, P. Mistriotis, A. C. N. Vasconcelos, E. E. Dixon, J. Yang, M. Benson, D. Maity, R. Walker, L. Martin, F. Koroma, F. Qian, K. Konstantopoulos, O. M. Woodward, S. X. Sun, Kidney epithelial cells are active mechano-biological fluid pumps. *Nat. Commun.* **13**, 2317 (2022).
59. X. Zhao, Y. Kong, B. Liang, J. Xu, Y. Lin, N. Zhou, J. Li, B. Jiang, J. Cheng, C. Li, W. Wang, Mechanosensitive Piezo1 channels mediate renal fibrosis. *JCI Insight* **7**, e152330 (2022).
60. E. Katsyuba, A. Mottis, M. Zietak, F. De Franco, V. van der Velpen, K. Gariani, D. Ryu, L. Cialabrini, O. Matilainen, P. Liscio, N. Giacchè, N. Stokar-Regenscheit, D. Legouis, S. de Seigneux, J. Ivanisevic, N. Raffaelli, K. Schoonjans, R. Pellicciari, J. Auwerx, De novo NAD$^+$ synthesis enhances mitochondrial function and improves health. *Nature* **563**, 354–359 (2018).
61. Z. Nadour, C. Simian, O. Laprévote, M. A. Loriot, I. A. Larabi, N. Pallet, Validation of a liquid chromatography coupled to tandem mass spectrometry method for simultaneous quantification of tryptophan and 10 key metabolites of the kynurenine pathway in plasma and urine: Application to a cohort of acute kidney injury patients. *Clin. Chim. Acta* **534**, 115–127 (2022).
62. M. T. Tran, Z. K. Zsengeller, A. H. Berg, E. V. Khankin, M. K. Bhasin, W. Kim, C. B. Clish, I. E. Stillman, S. A. Karumanchi, E. P. Rhee, S. M. Parikh, PGC1α drives NAD biosynthesis linking oxidative metabolism to renal protection. *Nature* **531**, 528–532 (2016).
63. T. Doke, S. Mukherjee, D. Mukhi, P. Dhillon, A. Abedini, J. G. Davis, K. Chellappa, B. Chen, J. A. Baur, K. Susztak, NAD$^+$ precursor supplementation prevents mtRNA/RIG-I-dependent inflammation during kidney injury. *Nat. Metab.* **5**, 414–430 (2023).
64. Y. Guan, S.-R. Wang, X.-Z. Huang, Q.-H. Xie, Y.-Y. Xu, D. Shang, C.-M. Hao, Nicotinamide mononucleotide, an NAD$^+$ precursor, rescues age-associated susceptibility to AKI in a Sirtuin 1-dependent manner. *J. Am. Soc. Nephrol.* **28**, 2337–2352 (2017).
65. M. V. Damgaard, J. T. Treebak, What is really known about the effects of nicotinamide riboside supplementation in humans. *Sci. Adv.* **9**, eadi4862 (2023).
66. K. F. Mills, S. Yoshida, L. R. Stein, A. Grozio, S. Kubota, Y. Sasaki, P. Redpath, M. E. Migaud, R. S. Apte, K. Uchida, J. Yoshino, S. I. Imai, Long-term administration of nicotinamide mononucleotide mitigates age-associated physiological decline in mice. *Cell Metab.* **24**, 795–806 (2016).
67. M. Yoshino, J. Yoshino, B. D. Kayser, G. J. Patti, M. P. Franczyk, K. F. Mills, M. Sindelar, T. Pietka, B. W. Patterson, S. I. Imai, S. Klein, Nicotinamide mononucleotide increases muscle insulin sensitivity in prediabetic women. *Science* **372**, 1224–1229 (2021).
68. B. Liao, Y. Zhao, D. Wang, X. Zhang, X. Hao, M. Hu, Nicotinamide mononucleotide supplementation enhances aerobic capacity in amateur runners: A randomized, double-blind study. *J. Int. Soc. Sports Nutr.* **18**, 54 (2021).
69. J. Irie, E. Inagaki, M. Fujita, H. Nakaya, M. Mitsuishi, S. Yamaguchi, K. Yamashita, S. Shigaki, T. Ono, H. Yukioka, H. Okano, Y.-I. Nabeshima, S.-I. Imai, M. Yasui, K. Tsubota, H. Itoh, Effect of oral administration of nicotinamide mononucleotide on clinical parameters and nicotinamide metabolite levels in healthy Japanese men. *Endocr. J.* **67**, 153–160 (2020).
70. M. Morgenstern, C. D. Peikert, P. Lübbert, I. Suppanz, C. Klemm, O. Alka, C. Steiert, N. Naumenko, A. Schendzielorz, L. Melchionda, W. W. D. Mühlhäuser, B. Knapp, J. D. Busch, S. B. Stiller, S. Dannenmaier, C. Lindau, M. Licheva, C. Eickhorst, R. Galbusera, R. M. Zerbes, M. T. Ryan, C. Kraft, V. Kozjak-Pavlovic, F. Drepper, S. Dennerlein, S. Oeljeklaus, N. Pfanner, N. Wiedemann, B. Warscheid, Quantitative high-confidence human mitochondrial proteome and its dynamics in cellular context. *Cell Metab.* **33**, 2464–2483.e18 (2021).
71. M. J. Waring, J. Arrowsmith, A. R. Leach, P. D. Leeson, S. Mandrell, R. M. Owen, G. Pairaudeau, W. D. Pennie, S. D. Pickett, J. Wang, O. Wallace, A. Weir, An analysis of the attrition of drug candidates from four major pharmaceutical companies. *Nat. Rev. Drug Discov.* **14**, 475–486 (2015).
72. Á. Duffy, M. Verbanck, A. Dobbyn, H.-H. Won, J. L. Rein, I. S. Forrest, G. Nadkarni, G. Rocheleau, R. Do, Tissue-specific genetic features inform prediction of drug side effects in clinical trials. *Sci. Adv.* **6**, eabb6242 (2020).
73. P. A. Nguyen, D. A. Born, A. M. Deaton, P. Nioi, L. D. Ward, Phenotypes associated with genes encoding drug targets are predictive of clinical trial side effects. *Nat. Commun.* **10**, 1579 (2019).
74. E. H. Yang, S. Shah, J. M. Criley, Digitalis toxicity: A fading but crucial complication to recognize. *Am. J. Med.* **125**, 337–343 (2012).
75. W. Amjad, W. Qureshi, A. Farooq, U. Sohail, S. Khatoon, S. Pervaiz, P. Narra, S. M. Hasan, F. Ali, A. Ullah, S. Guttmann, Gastrointestinal side effects of antiarrhythmic medications: A review of current literature. *Cureus* **9**, e1646 (2017).
76. Y.-K. Wang, N. Ma, S. Xu, J.-Y. Huang, Q.-Z. Ni, H.-J. Cao, Q.-W. Zheng, B. Zhu, J. Xia, F.-K. Zhang, X.-F. Ding, X.-S. Qiu, T.-W. Chen, K. Wang, W. Chen, Z.-G. Li, S.-Q. Cheng, D. Xie, J.-J. Li, PPDPF suppresses the development of hepatocellular carcinoma through TRIM21-mediated ubiquitination of RIPK1. *Cell Rep.* **42**, 112340 (2023).
77. L. Ho, D. Zhao, K. Ono, K. Ruan, I. Mogno, M. Tsuji, E. Carry, J. Brathwaite, S. Sims, T. Frolinger, S. Westfall, P. Mazzola, Q. Wu, K. Hao, T. E. Lloyd, J. E. Simon, J. Faith, G. M. Pasinetti, Heterogeneity in gut microbiota drive polyphenol metabolism that influences alpha-synuclein misfolding and toxicity. *J. Nutr. Biochem.* **64**, 170–181 (2019).
78. M. Pertea, D. Kim, G. M. Pertea, J. T. Leek, S. L. Salzberg, Transcript-level expression analysis of RNA-seq experiments with HISAT, stringtie and ballgown. *Nat. Protoc.* **11**, 1650–1667 (2016).
79. M. I. Love, W. Huber, S. Anders, Moderated estimation of fold change and dispersion for RNA-seq data with DESeq2. *Genome Biol.* **15**, 550 (2014).
80. Y. T. Guan, Y. L. Ma, Q. Li, Z. L. Sun, L. Ma, L. J. Wu, L. R. Wang, L. Zeng, Y. J. Shao, Y. T. Chen, N. Ma, W. Q. Lu, K. W. Hu, H. H. Han, Y. H. Yu, Y. H. Huang, M. Y. Liu, D. L. Li, CRISPR/Cas9-mediated somatic correction of a novel coagulator factor IX gene mutation ameliorates hemophilia in mouse. *EMBO Mol. Med.* **8**, 477–488 (2016).
81. Y. Guan, X. Liang, Z. Ma, H. Hu, H. Liu, Z. Miao, A. Linkermann, J. N. Hellwege, B. F. Voight, K. Susztak, A single genetic locus controls both expression of and kidney disease development via ferroptosis. *Nat. Commun.* **12**, 5078 (2021).
82. S. G. Tullius, H. R. C. Biefer, S. Li, A. J. Trachtenberg, K. Edtinger, M. Quante, F. Krenzien, H. Uehara, X. Yang, H. T. Kissick, W. P. Kuo, I. Ghiran, M. A. de la Fuente, M. S. Arredouani, V. Camacho, J. C. Tigges, V. Toxavidis, R. E. Fatimy, B. D. Smith, A. Vasudevan, A. ElKhal, NAD$^+$ protects against EAE by regulating CD4$^+$ T-cell differentiation. *Nat. Commun.* **5**, 5101 (2014).
83. P. M. Quiros, A. Goyal, P. Jha, J. Auwerx, Analysis of mtDNA/nDNA ratio in mice. *Curr. Protoc. Mouse Biol.* **7**, 47–54 (2017).
84. L. Wang, Y. Shao, Y. Guan, L. Li, L. Wu, F. Chen, M. Liu, H. Chen, Y. Ma, X. Ma, M. Liu, D. Li, Large genomic fragment deletion and functional gene cassette knock-in via Cas9 protein mediated genome editing in one-cell rodent embryos. *Sci. Rep.* **5**, 17517 (2015).

Acknowledgments: We thank the East China Normal University Multifunctional Platform for Innovation (011). We thank the bioinformation suggestion from S. Fan of Fudan University. **Funding:** This work was supported by National Key Research and Development Program of China (2022YFC2505400 and 2022YFC3400203 to Y.G. and 2024YFC3406700 to H.G.), National Natural Science Foundation of China (82100773 and 32470823 to Y.G., 82101486 and 82371426 to Q.W., and 62102115 to X.Y.), Shanghai Rising-Star Program (22QA1405900 to Y.G.), Natural Science Foundation of Chongqing, China (CSTB2022NSCQ-MSX1621 to Y.G.), Ningxia Hui Autonomous Region Key Research and Development Project (2022BFH02012 to Q.W.), Shanghai Fourth People's Hospital affiliated to Tongji University School of Medicine (sykyqd02301 and sykyqd02302 to Q.W.), the Fundamental Research Funds for the Central Universities (to Q.W.), and Science and Technology Commission of Shanghai Municipality (STCSM) grant (23ZR1467900 to Q.W.), the Fundamental Research Funds for the Central Universities at Harbin Engineering University (3072024GH2604 to X.Y.), the Shandong Provincial Natural Science Foundation (2022HWYQ-093 to X.Y.), and Foundation of Children's Hospital of Fudan University (EKYX202423 to R.Z. and EKSJD202416 to X.F.).
Author contributions: Y.G. and H.G., conceived and led this study. R.Z. performed the single-cell sequencing experiment. Y.Z., D.Z., and Y.G. performed animal studies. Y.Z. and Y.G. performed cell culture experiments. X.F., K.W., F.Z., and K.L. performed histological analysis. Q.W., Y.L., and Y.W. performed redox analysis. Q.W., X.Y., X.L., and W.D. performed computation analysis. Q.H.X.L. performed NAD$^+$ probe experiments. X.F., G.X., N.L., J.N., and D.L. analyzed the data. Q.W. and Y.G. wrote the paper. All authors read and approved the manuscript. **Competing interests:** The authors declare that they have no competing interests. **Data and materials availability:** The sequencing data used in this study are available in the NCBI's Sequence Read Archive (SRA) database under accession code PRJNA1028147 (https://ncbi.nlm.nih.gov/bioproject/PRJNA1028147). All other data needed to evaluate the conclusions in the paper are present in the paper and/or the Supplementary Materials.

Submitted 18 July 2024
Accepted 24 December 2024
Published 19 March 2025
10.1126/sciadv.adr8648